

Dust Growth in ALMA Rings: II. Dusty Rossby Wave Instability

CAN CUI,^{1,2,*} KONSTANTIN GERBIG,³ YA-PING LI,⁴ ZIYAN XU,⁵ RIXIN LI,⁶ CONG YU,⁷ MIN-KAI LIN,^{8,9} AND
FENG YUAN¹⁰

¹*Department of Astronomy and Astrophysics, University of Toronto, Toronto, ON M5S 3H4, Canada*

²*Institute for Deep Space Exploration, Nanjing University, Suzhou 215163, China*

³*Department of Astronomy, Yale University, New Haven, CT 06511, USA*

⁴*Shanghai Astronomical Observatory, Chinese Academy of Sciences, Shanghai 200030, China*

⁵*Center for Star and Planet Formation, GLOBE Institute, University of Copenhagen, Øster Voldgade 5–7, 1350 Copenhagen, Denmark*

⁶*Department of Astronomy, Theoretical Astrophysics Center, and Center for Integrative Planetary Science,
University of California Berkeley, Berkeley, CA 94720-3411, USA*

⁷*School of Physics and Astronomy, Sun Yat-Sen University, Zhuhai 519082, China*

⁸*Institute of Astronomy and Astrophysics, Academia Sinica, Taipei 10617, Taiwan, R.O.C.*

⁹*Physics Division, National Center for Theoretical Sciences, Taipei 10617, Taiwan, R.O.C.*

¹⁰*Center for Astronomy and Astrophysics and Department of Physics, Fudan University, 200438, Shanghai, China*

ABSTRACT

Annular substructures serve as ideal venues for planetesimal formation. In this series, we investigate the linear stage of dust growth within rings. The first paper examines the global streaming instability, while this study focuses on the dusty Rossby wave instability (DRWI). We perform a linear analysis of the two-fluid equations on a background pressure bump, representing annular substructures. The spectral code DEDALUS is used to solve the linear eigenvalue problem. We identify two distinct DRWI modes: Type I, which originates from dust-modified gas RWI, and Type II, which results from dust-gas coupling. These modes never coexist for a given azimuthal wavenumber k_y , but transition between each other as k_y varies. Type I modes are driven by the advection of background vorticity, whereas Type II modes involve two primary waves: Rossby waves, driven by advection, and thin waves, driven by dust-gas drag. Finally, we assess the relevance of DRWI in ALMA rings using DSHARP sources. Our findings suggest that Type I modes could explain the absence of azimuthal asymmetries in many ALMA disks, whereas Type II modes are entirely absent in all eight observed rings, implying that unresolved narrow rings or alternative mechanisms may play a role in dust growth within annular substructures.

Keywords: Hydrodynamics — Instabilities — Protoplanetary disks — Planet formation

1. INTRODUCTION

Protoplanetary disks are the birth places of planets, where dust particles coagulate and collapse into planetesimals, seeding further growth into terrestrial planets and cores of gas giants. Planet formation requires the growth from micron-sized dust into $\sim 10^3 - 10^5$ km-sized planets within several million years (Simon et al. 2022; Drażkowska et al. 2023). In the early stage of planet formation, laboratory experiments have showed that grains of $0.1 - 1 \mu\text{m}$ in size generally stick and grow upon mutual collisions (Blum & Wurm 2008; Gundlach & Blum 2015; Blum 2018). The outcome of sticking can

yield cm-sized grains at 1 AU (Zsom et al. 2010), and mm-sized grains at $\sim 15 - 50$ AU (Lorek et al. 2018). The intermediate stage of planet formation is the conversion of mm- to cm-sized grains, or pebbles, to km-sized planetesimals. However, the growth by sticking is halted by the bouncing or fragmentation barrier in the inner part of the disk (Güttler et al. 2010; Zsom et al. 2010), and by the fast radial drift barrier in the outer part of the disk (Weidenschilling 1977; Birnstiel et al. 2010; Birnstiel 2024). Observations of dust continuum emission provide insights into overcoming the growth barriers. Below, we discuss two disk substructures and how they may serve as favorable sites for dust growth.

1.1. Planetesimal Formation in Dust Rings

* ccui@nju.edu.cn

The Atacama Large Millimeter/submillimeter Array (ALMA) uncovered a diverse range of disk substructures in the (sub)millimeter dust continuum, among which rings and gaps are the most ubiquitous (Andrews et al. 2018; Huang et al. 2018a; Andrews 2020). These rings are commonly identified as likely venues for planetesimal formation (e.g., Stammer et al. 2019), and can be formed and maintained by numerous mechanisms, such as planet-disk interactions (Goldreich & Tremaine 1979; Lin & Papaloizou 1986, 1993; Keppler et al. 2018; Haffert et al. 2019; Pinte et al. 2023; Bae et al. 2023). To collect dust particles within rings, gas pressure bumps are typically required, as dust naturally migrates towards pressure maxima. These local pressure bumps have been seen in many numerical simulations with a planet carving one or multiple gaps (e.g., Pinilla et al. 2012; Dong et al. 2015). Furthermore, since dust particles within are expected to experience turbulent diffusion (Dullemond et al. 2018, hereafter D+18, Rosotti et al. 2020), dust rings have finite widths, as otherwise, particles would concentrate towards pressure maxima indefinitely.

The streaming instability (SI) (Youdin & Goodman 2005) is the leading mechanism for overcoming the bouncing, fragmentation, and radial drift barriers in planetesimal formation. The linear SI exhibits fastest growth rates when the relative drift velocity between the gas and dust induced by the background gas pressure gradient is in resonance with the phase velocity of an inertial wave (Squire & Hopkins 2018a,b; Magnan et al. 2024). The linear SI amplifies perturbations particularly fast for dust-to-gas ratios of unity or greater, and for marginally coupled particles, i.e. grains with stopping time t_s comparable to the local dynamical time scale Ω^{-1} , or, in other words, a Stokes number $St \equiv t_s \Omega$ close to unity. Indeed, mm- or cm-sized solids that inhabit the top end of the expected dust size distribution in protoplanetary disks, possess a Stokes number of $St \sim 0.1 - 1$. For such grains, the non-linear outcome of SI is characterized by strong, and rapidly emerging clumping of solids, within several local orbital timescales (e.g., Johansen et al. 2007; Bai & Stone 2010; Carrera et al. 2015; Yang et al. 2017; Li et al. 2019; Gerbig et al. 2020; Schäfer et al. 2024). When particle clumps reach the Roche density, dust self-gravity enables the formation of planetesimals with $\sim 10 - 100$ km in size (e.g., Johansen et al. 2015; Simon et al. 2016; Schäfer et al. 2017; Klahr & Schreiber 2020; Gerbig & Li 2023).

However, the picture of planetesimal formation in diffusive dust rings mediated by SI faces two problems. First, the presence of turbulent diffusion reduces the growth rate of the linear SI (Umurhan et al. 2020; Chen & Lin 2020), and may inhibit particle clumping dur-

ing non-linear SI as seen in numerical simulations (with forced turbulence of $\alpha \sim 10^{-3}$) (Lim et al. 2024). Second, the pressure gradient vanishes at the center of a dust ring, removing the relative drift between gas and dust and depriving the SI of its energy source. If the dust layer is subjected to appreciable levels of gas turbulence, it will nonetheless have a finite thickness, yet now without the ability to clump via drag instabilities, and is thus unable to form planetesimals.

On the other hand, recent local non-ideal MHD shearing box simulations have demonstrated that particle clumping may be possible in pressure maxima (Xu & Bai 2022a,b), if induced by MRI zonal flows that are commonly seen in MHD simulations (e.g., Johansen et al. 2009; Bai & Stone 2014; Riols & Lesur 2019; Cui & Bai 2021, 2022; Hu et al. 2022). Therefore, it is of importance to explore that, in the context of a pressure bump, 1) whether SI can still operate, and 2) whether new instabilities can set in to enhance local dust-to-gas ratio.

1.2. Planetesimal Formation in Azimuthal Dust Clumps

Azimuthal crescent-shaped dust clumps have been observed in continuum of a handful of protoplanetary disks (e.g. van der Marel et al. 2013; Huang et al. 2018a; Andrews 2020; van der Marel et al. 2021). The crescent clumps are considered to be indicative of large, and potentially long-lived gas vortices. Similar to rings, these crescents provide ideal sites for overcoming the growth barriers by trapping particles now at the pressure maxima of vortices (Barge & Sommeria 1995). The Rossby wave instability (RWI) is a promising mechanism to drive such large, lopsided vortices (Lovelace et al. 1999), as seen in numerical simulations of the RWI's non-linear evolution (Li et al. 2001). The necessary condition of RWI is local extrema in the radial vortensity profile (Lovelace et al. 1999; Li et al. 2000; Chang & Youdin 2024). Such local extrema can be readily produced by planets, due to a sharp transition in radial gas density at gap edges. Numerical simulations have indeed found the excitation of vortices in this context (Zhu et al. 2014; Zhu & Stone 2014; Hammer et al. 2017; Huang et al. 2018b; Li et al. 2020; Cimerman & Rafikov 2023; Ma et al. 2024).

The classic RWI is a purely gas-driven instability. While numerical investigations have shown that its non-linear saturation, RWI effectively generates vortices and traps particles, its linear theory did not account for aerodynamic drag until very recently. Liu & Bai (2023, hereafter LB23) is the first work to consider the effect of particles onto the RWI. As a pioneering study, they adopted a single-fluid formulation, where gas and dust

were treated as one fluid (Lin & Youdin 2017). In a radially global shearing box, they employed a pressure bump background state mimicking the gas distribution of a ring, and discovered two distinct modes of the Dusty RWI (DRWI). Type I modes are similar to the gas RWI, in that growth rates peak for pure gas and decrease with increasing dust-to-gas mass ratio. Type II modes are novel and rely on the presence of dust. Moreover, LB23 performed shearing box simulations (on H -scales radially) to verify their linear theory and found that, while for Type I, the background dust ring structure is disrupted and vortices like gas RWI emerge, for Type II, the background ring persists and facilitate dust clumping. Thus, they concluded that Type II DRWI may be a new mechanism that can enhance local dust-to-gas ratios and promote planetesimal formation in protoplanetary disk rings seen by ALMA.

In the end of §1.1, we discuss two directions that worth investigating at the location of ALMA rings (pressure bumps). The global linear analysis of the streaming instability in a pressure bump is explored in the first paper. In this study, we focus on the second direction by exploring the DRWI using a two-fluid formulation. The paper is organized as follows. In §2, we introduce the basic equations and disk model. §3 details the numerical method used. In §4, we present the growth rates found for Type I and Type II DRWI modes. In §5, we apply parameters from DSHARP sources to the linear analysis and discuss the onset of DRWI in ALMA rings. Finally, we summarize the main findings in §6.

2. METHODS

In this section, we present the basic equations and disk model. Specifically, they are dynamical equations (2.1), definition of parameters (2.2), disk model (2.3), equilibrium solutions (2.4), and linearized equations (2.5).

2.1. Dynamical Equations

We employ the unstratified shearing sheet approximation (Goldreich & Lynden-Bell 1965; Latter & Papaloizou 2017), which is a Cartesian representation of a small patch in the global disk. It is centered at $(r_0, \phi_0 = \Omega t, z_0 = 0)$, and rotates around the central star with mass M at Keplerian angular velocity $\Omega = \Omega_K(r_0)$. Cartesian coordinates (x, y, z) denote radial, azimuthal, and vertical directions. Keplerian velocity appears as a linear shear in the shearing box, $-q\Omega x \mathbf{e}_y$ with $q = 3/2$. Moreover, we consider a two-fluid protoplanetary disk composed of gas and dust. The gas density, velocity, and pressure are denoted by $(\rho_g, \mathbf{v}_g, P)$, and the pressureless (Lynch & Laibe 2024), single-species dust has density and velocity denoted by (ρ_d, \mathbf{v}_d) .

The dynamical equations of the gas-dust two-fluid framework are,

$$\frac{\partial \rho_g}{\partial t} + \nabla \cdot (\rho_g \mathbf{v}_g) = 0, \quad (1)$$

$$\frac{\partial \rho_d}{\partial t} + \nabla \cdot (\rho_d \mathbf{v}_d) = 0, \quad (2)$$

$$\begin{aligned} \frac{\partial \mathbf{v}_g}{\partial t} + \mathbf{v}_g \cdot \nabla \mathbf{v}_g = & -\frac{\nabla P}{\rho_g} - 2\boldsymbol{\Omega} \times \mathbf{v}_g + 3\Omega^2 x \mathbf{e}_x + \frac{\epsilon}{t_s}(\mathbf{v}_d - \mathbf{v}_g) \\ & + \nu \nabla^2 \mathbf{v}_g + F(x) \mathbf{e}_y, \end{aligned} \quad (3)$$

$$\begin{aligned} \frac{\partial \mathbf{v}_d}{\partial t} + \mathbf{v}_d \cdot \nabla \mathbf{v}_d = & -2\boldsymbol{\Omega} \times \mathbf{v}_d + 3\Omega^2 x \mathbf{e}_x - \frac{1}{t_s}(\mathbf{v}_d - \mathbf{v}_g) \\ & + \frac{1}{\rho_d} \nabla \cdot (\rho_d \mathbf{v}_{\text{dif}} \mathbf{v}_{\text{dif}}). \end{aligned} \quad (4)$$

In the above, $\epsilon = \rho_d/\rho_g$ is the dust-to-gas mass ratio, t_s is the particle stopping time, ν is the kinematic viscosity, \mathbf{v}_{dif} is the dust diffusion velocity, and $F(x)$ is a forcing term in the y -direction. See the definitions of these parameters in §2.2 and §2.4.1. The equation of state is set to be locally isothermal,

$$P = \rho_g c_s^2, \quad (5)$$

and c_s denotes the isothermal sound speed. The units throughout are chosen to be $GM = \rho_0 = r_0 = 1$. The gas pressure scale height is defined as $H \equiv c_s/\Omega$, with $H/r_0 = 0.05$.

2.2. Definition of Parameters

Dust dynamics is strongly affected by the coupling to the gas via the drag force in protoplanetary disks. For a large portion of the disk and particle sizes, the mean free path of the gas molecules is greater than the particle radius. This is called the Epstein drag law regime (Epstein 1924). The particle stopping time, a timescale for the decay of the relative velocity between the dust and gas due to the drag force, in the Epstein regime is

$$t_s = \frac{\rho_s a}{\rho_g v_{\text{th}}}, \quad (6)$$

where ρ_s is the material density of the particle, a is the radius of the particle (treated as a hard sphere), and $v_{\text{th}} = \sqrt{8/\pi} c_s$ is the gas mean thermal velocity (Birnstiel 2024). Since we consider the motions of dust in the gas disk, the relevant timescale is the orbital period. Thereby, it is useful to define a dimensionless stopping time, or the so called Stokes number

$$\text{St} = t_s \Omega. \quad (7)$$

In this work, we focus on the regime where the dust and gas are well-coupled ($\text{St} \ll 1$), in order to be consistent with the non-drift steady state solution adopted in §2.4.1.

Turbulent diffusion is a significant physical quantity in the context of annular substructures, as it determines the width of a ring (D+18). Without it, dust particles will continue to migrate indefinitely towards the pressure maxima. In this work, gas turbulence is modeled by a viscous term in Equation (3), where $\nu = \alpha c_s H$ is the kinematic viscosity, and α is the Shakura-Sunyaev parameter (Shakura & Sunyaev 1973). The dust diffusion term in Equation (4) is modeled by the Reynolds-averaged mean-flow method, with a gradient diffusion approach to close the system (Binkert 2023). The dust diffusion velocity is expressed by (LB23),

$$\mathbf{v}_{\text{dif}} = -D_d \frac{\rho_g}{\rho_d} \nabla \frac{\rho_d}{\rho_g}, \quad (8)$$

where D_d is the particle diffusion coefficient. We note that in equations (1)-(4), \mathbf{v}_d involves the dust velocity and the dust diffusion velocity \mathbf{v}_{dif} . Hence, the drag force terms includes the dust diffusion velocity.

It is common to relate the gas diffusion coefficient to particle diffusion coefficient (Youdin & Lithwick 2007). We treat dust and gas diffusion coefficients to be equal and constants, $D_d = \nu = \text{const.}$ Note that this approximation is only strictly valid when $\text{St} \ll 1$, because $\nu/D_d \sim 1 + \text{St}^2$ (Youdin & Lithwick 2007).

2.3. Disk Model

The disk model is established with a symmetric bump centered at $x = 0$. The bump is specified by a Gaussian profile in the gas density and pressure,

$$\rho_{g0} = \rho_0 \left[1 + A \exp \left(-\frac{x^2}{2w^2} \right) \right]. \quad (9)$$

Here, ρ_0 , A , w denote background gas density, bump amplitude and width. The fiducial parameters are $A = 1.5$ and $w = H$. Such a Gaussian bump can produce vortensity extrema in x , which is a necessary condition to excite the gas RWI (Chang & Youdin 2024).

Background dust density can be obtained by setting up the disk equilibrium (§2.4.1), and is shown in Figure 1. However, to ease the calculations, rather than directly using the dust density computed from equilibrium, we approximate the results with a Gaussian profile,

$$\rho_{d0*} = \rho_0 \max \left[A_d \exp \left(-\frac{x^2}{2w_d^2} \right), 0.01 \right], \quad (10)$$

where $A_d = \epsilon_{\text{max}}(1 + A)$, and ϵ_{max} is the background dust-to-gas mass ratio at the bump center. The Gaussian profile is the analytical solution to the dust trapping problem (D+18). For locations far from the bump

center, we require $\epsilon = 0.01$. This is done by setting a minimum $\rho_{d0*} = 0.01$, as the minimum gas density $\rho_{g0} \sim 1$.

2.4. Equilibrium Solutions

In the steady state, temporal derivatives vanish ($\partial/\partial t = 0$), and axisymmetry is assumed ($\partial/\partial y = 0$). Equations (1)-(4) then become

$$\frac{\partial v_{\text{gx}}}{\partial x} = -\frac{\partial \ln \rho_g}{\partial x} v_{\text{gx}}, \quad (11)$$

$$\frac{\partial v_{\text{dx}}}{\partial x} = -\frac{\partial \ln \rho_d}{\partial x} v_{\text{dx}}, \quad (12)$$

$$\begin{aligned} v_{\text{gx}} \frac{\partial v_{\text{gx}}}{\partial x} = & -\frac{1}{\rho_g} \frac{\partial P}{\partial x} + 2\Omega v_{\text{gy}} + 3\Omega^2 x + \nu \frac{\partial^2 v_{\text{gx}}}{\partial x^2} \\ & + \frac{\epsilon}{t_s} (v_{\text{dx}} - v_{\text{gx}}), \end{aligned} \quad (13)$$

$$v_{\text{gx}} \frac{\partial v_{\text{gy}}}{\partial x} = -2\Omega v_{\text{gx}} + \nu \frac{\partial^2 v_{\text{gy}}}{\partial x^2} + \frac{\epsilon}{t_s} (v_{\text{dy}} - v_{\text{gy}}) + F, \quad (14)$$

$$\begin{aligned} v_{\text{dx}} \frac{\partial v_{\text{dx}}}{\partial x} = & +2\Omega v_{\text{dy}} + 3\Omega^2 x + \frac{1}{\rho_d} \frac{\partial}{\partial x} [\rho_d D_d^2 (\partial \ln \epsilon / \partial x)^2] \\ & - \frac{1}{t_s} (v_{\text{dx}} - v_{\text{gx}}), \end{aligned} \quad (15)$$

$$v_{\text{dx}} \frac{\partial v_{\text{dy}}}{\partial x} = -2\Omega v_{\text{dx}} - \frac{1}{t_s} (v_{\text{dy}} - v_{\text{gy}}), \quad (16)$$

where we drop the subscription ‘0’ for equilibrium quantities to simplify the notation.

In the subsection below, we derive the non-drift steady state solution, that is different from the drift solution adopted in Youdin & Goodman (2005) for SI. By ignoring viscosity and forcing ($\nu = F = D_d = 0$), eqs. (11)-(16) resemble the steady state equations of SI (Youdin & Goodman 2005). The solution of it was adopted from Nakagawa et al. (1986), which contains a velocity drift between gas and dust, with relative radial velocity $\sim O(\text{St}f)$ and relative azimuthal velocity $\sim O(\text{St}^2 f^2)$, when $\text{St}^2 f^2 \ll 1$, where $f = \rho_g/(\rho_g + \rho_d)$. While the onset of SI relies on the relative drift between gas and dust, this is not required for the (D)RWI, because the classic RWI only involves the gas component (Lovelace et al. 1999). In fact, our non-drift solution effectively filters out the SI.

2.4.1. Non-Drift Solution

We present a simple solution to equations (11)-(16) without velocity drift. This non-drift solution reads

$$v_{\text{gx}0} = v_{\text{dx}0} = 0, \quad v_{\text{gy}0} = v_{\text{dy}0}. \quad (17)$$

Physically, it corresponds to a regime where the Stokes number is sufficiently small. As we will discuss in §4, the two types of DRWI modes exhibit more intriguing behaviors when $St \leq 1$. For $St = 10$, the growth rates closely resemble those of the classic gas RWI. However, it is important to note that, strictly speaking, our results are only valid in the regime $Stf \ll 1$. To further simplify the solution, we impose the condition that both radial velocities vanish in gas and dust. Consequently, all the left hand sides of momentum equations become zero. Now, equations (11)-(16) are simplified to three relations, where $v_{gy0}, v_{dy0}, F, \rho_{d0}$ can be computed.

First, the steady state y -velocities can be directly found by Equation (13),

$$v_{gy0} = v_{dy0} = -\frac{3}{2}\Omega x + \frac{1}{2\Omega} \frac{1}{\rho_{g0}} \frac{\partial P_0}{\partial x}. \quad (18)$$

This is simply the standard Keplerian profile with a pressure gradient on top of it, commonly seen in the pure gas system. In a pressure bump, the y -velocity is sub-Keplerian for $x > 0$ and super-Keplerian for $x < 0$. Second, the forcing F is used to balance the turbulent diffusion due to the shear of v_{gy} in x . By Equations (14) and (18), F is given by

$$F(x) = -\nu \frac{\partial^2 v_{gy0}}{\partial x^2} = -\nu \frac{c_s^2}{2\Omega} \frac{\partial^3 \ln \rho_{g0}}{\partial x^3}. \quad (19)$$

Since $F(x)$ is a forcing term, it only appears in the steady states, but not involved in the linearized equations.

Lastly, dust density profile ρ_d can be computed by comparing the dust diffusion term in Equation (15) and the gas pressure gradient term in Equation (13). No relative drift between v_{gy} and v_{dy} indicates that these two terms should exactly equal,

$$\frac{1}{\rho_{d0}} \frac{\partial}{\partial x} [\rho_{d0} D_d^2 (\partial \ln \epsilon_0 / \partial x)^2] + \frac{1}{\rho_{g0}} \frac{\partial P_0}{\partial x} = 0. \quad (20)$$

Dust density profile is computed by solving the above ordinary differential equation (ODE) as an initial value problem (IVP), where the initial condition is given at the center of the box (slightly shifted from $x = 0$ to avoid singularity), and the IVP is solved for $x > 0$. The detailed numerical method of solving this ODE can be found in Appendix A.

Figure 1 shows the gas and dust density distributions. The gas density (ρ_{g0}) is directly plotted from Equation (9). The dust density (ρ_{d0}) is obtained by solving Equation (20), for different levels of turbulence $\alpha \in [10^{-3}, 10^{-2}, 10^{-1}]$ from left to right (Rosotti 2023), and dust-to-gas mass ratios $\epsilon_{\max} \in [0.5, 0.3, 0.1]$ from high to low. Note that our ρ_{d0} does not depend on the

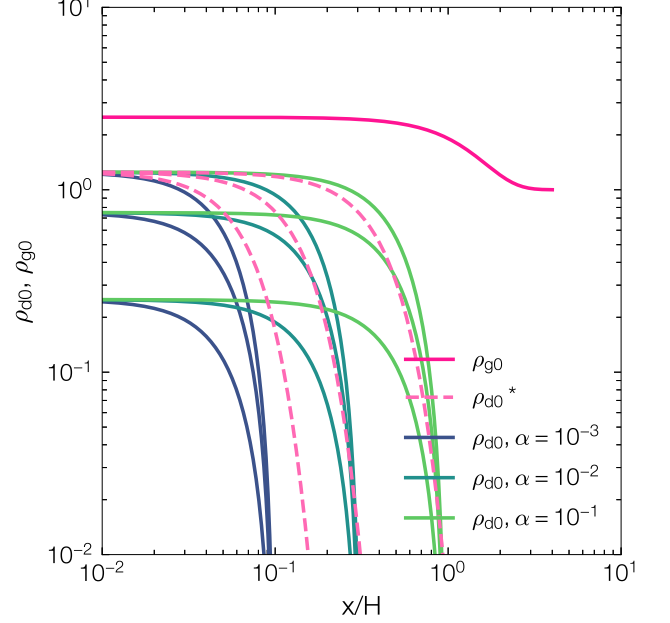


Figure 1. Gas and dust density distributions in log-log scale. Gas density (ρ_{g0}) is plotted with Equation (9) (solid pink). Dust density (ρ_{d0}) is plotted by solving Equation (20) (green and blue), for different turbulence levels $\alpha \in [10^{-3}, 10^{-2}, 10^{-1}]$ (left to right) and dust-to-gas mass ratios $\epsilon_{\max} \in [0.5, 0.3, 0.1]$ (high to low). The dashed lines show ρ_{d0*} defined in Equation (10) with $w_d/H \in [0.05, 0.1, 0.3]$ at $\epsilon_{\max} = 0.5$ (left to right).

Stokes number, because there is no drift in equilibrium. Dashed pink curves denote $w_d/H \in [0.05, 0.1, 0.3]$ from left to right for ρ_{d0*} defined in Equation (10). For simplicity, we utilize ρ_{d0*} rather than ρ_{d0} computed from IVP as the equilibrium dust density when conducting the linear analysis throughout this work. Our tests show that the Gaussian dust density profile (dashed curves) does not qualitatively alter the results compared to the numerically computed profile (solid green curves).

2.5. Linearized Equations

Consider small perturbations to eqs. (1)-(4), such that for example, $\mathbf{v} = \mathbf{v}_0 + \delta\mathbf{v}(x, y, t)$, $\rho = \rho_0 + \delta\rho(x, y, t)$. We linearize these equations by considering Eulerian perturbations $\propto f(x) \exp(ik_y y - i\omega t)$, where k_y is the y -wavenumber, and $\omega = \omega_r + i\gamma$ is the mode frequency, where γ denotes the growth rate. We drop the subscription ‘0’ to simplify the notation for the linearized equations. The linearized continuity, momentum, and energy equations are

$$-i\Delta\omega\delta\rho_g + \frac{\partial[\rho_g\delta v_{gx}]}{\partial x} + ik_y\rho_g\delta v_{gy} = 0, \quad (21)$$

$$-i\Delta\omega_d\delta\rho_d + \frac{\partial[\rho_d\delta v_{dx}]}{\partial x} + ik_y\rho_d\delta v_{dy} = 0, \quad (22)$$

$$\begin{aligned} & -i\Delta\omega\delta v_{gx} - 2\Omega\delta v_{gy} + \frac{1}{\rho_g}\frac{\partial\delta P}{\partial x} - \frac{\delta\rho_g}{\rho_g^2}\frac{\partial P}{\partial x} \\ & - \nu\left(\frac{\partial^2}{\partial x^2} - k_y^2\right)\delta v_{gx} - \frac{1}{t_s}\frac{\rho_d}{\rho_g}(\delta v_{dx} - \delta v_{gx}) \\ & = 0, \end{aligned} \quad (23)$$

$$\begin{aligned} & -i\Delta\omega\delta v_{gy} + \delta v_{gx}\frac{\partial v_{gy}}{\partial x} + 2\Omega\delta v_{gx} + \frac{ik_y}{\rho_g}\delta P \\ & - \nu\left(\frac{\partial^2}{\partial x^2} - k_y^2\right)\delta v_{gy} - \frac{1}{t_s}\frac{\rho_d}{\rho_g}(\delta v_{dy} - \delta v_{gy}) \\ & = 0, \end{aligned} \quad (24)$$

$$-i\Delta\omega_d\delta v_{dx} - 2\Omega\delta v_{dy} + \frac{1}{t_s}(\delta v_{dx} - \delta v_{gx}) - D_{dx} = 0, \quad (25)$$

$$\begin{aligned} & -i\Delta\omega_d\delta v_{dy} + \delta v_{dx}\frac{\partial v_{dy}}{\partial x} + 2\Omega\delta v_{dx} + \frac{1}{t_s}(\delta v_{dy} - \delta v_{gy}) \\ & - D_{dy} = 0, \end{aligned} \quad (26)$$

$$\delta P = \delta\rho_g c_s^2, \quad (27)$$

where $\Delta\omega = \omega - k_y v_{gy}$ and $\Delta\omega_d = \omega - k_y v_{dy}$.

The linearized dust diffusion terms in equations (25) and (26) are

$$\begin{aligned} D_{dx} = & + \frac{1}{\rho_d}\frac{\partial}{\partial x}(2\rho_d v_{diffx} v'_{diffx} + \delta\rho_d v_{diffx}^2) \\ & - \frac{\delta\rho_d}{\rho_d^2}\frac{\partial}{\partial x}(\rho_d v_{diffx}^2) + ik_y v_{diffx} v'_{diffy}, \end{aligned} \quad (28)$$

$$D_{dy} = \frac{1}{\rho_d}\frac{\partial}{\partial x}(\rho_d v_{diffx} v'_{diffy}), \quad (29)$$

where the steady state and perturbed dust diffusion velocities are

$$v_{diffx} = D_d \frac{\rho_g}{\rho_d} \frac{\partial}{\partial x} \frac{\rho_d}{\rho_g}, \quad (30)$$

$$v_{diffy} = 0, \quad (31)$$

$$v'_{diffx} = D_d \left[\frac{\rho_g}{\rho_d} \frac{\partial}{\partial x} \left(\frac{\delta\rho_d}{\rho_g} - \frac{\rho_d\delta\rho_g}{\rho_g^2} \right) + \left(\frac{\delta\rho_g}{\rho_d} - \frac{\rho_g\delta\rho_d}{\rho_d^2} \right) \frac{\partial}{\partial x} \frac{\rho_d}{\rho_g} \right], \quad (32)$$

$$v'_{diffy} = D_d ik_y \left(\frac{\delta\rho_d}{\rho_d} - \frac{\delta\rho_g}{\rho_g} \right). \quad (33)$$

3. NUMERICS

We solve linearized equations numerically via the pseudospectral method (see e.g., Cui & Lin 2021; Cui et al. 2024), also known as the orthogonal collocation method. This technique approximates solutions to differential equations by a weighted sum of orthogonal basis functions, typically trigonometric functions or orthogonal polynomials, up to a certain degree (Boyd 2001). The linearized differential equations presented in §2.5 formulate the standard linear eigenvalue problem (EVP). In a generalized matrix form, it is written as

$$A\vec{x} = L\vec{x} + \omega M\vec{x} = 0, \quad (34)$$

where ω is the eigenvalue, and $\vec{x} = [\delta v_{gx}, \delta v_{gy}, \delta v_{dx}, \delta v_{dy}, \delta \rho_g, \delta \rho_d]^T$ is a vector of eigenfunctions with six perturbed quantities. Here, A , L , M are $6N \times 6N$ sized matrices, with L consists of linear operators.

We employ DEDALUS¹ a general purpose spectral code to solve the EVP (Burns et al. 2020). Fourier series are chosen as the orthogonal basis functions to expand the eigenfunctions, which naturally enforce periodic boundary conditions (a comparison of boundary conditions between this work and previous studies is provided in Appendix B). The computational domain spans $x \in [-4H, 4H]$ and is discretized into N points with uniform spacing. We employ the dense solver method via `solve_dense`, which converts matrix A into dense arrays, and utilize `scipy.linalg.eig` routine from Python, that can solve the EVP directly. A numerical resolution of $N = 251$ is adopted. The resolution is increased to $N = 401$ to ensure convergence and accuracy of the results when necessary.

4. RESULTS

4.1. Classic RWI

We begin by computing the linear growth rates of the pure gas RWI, using only the gas components of equations (11)–(16) within the compressible shearing sheet

¹ <https://dedalus-project.org/>

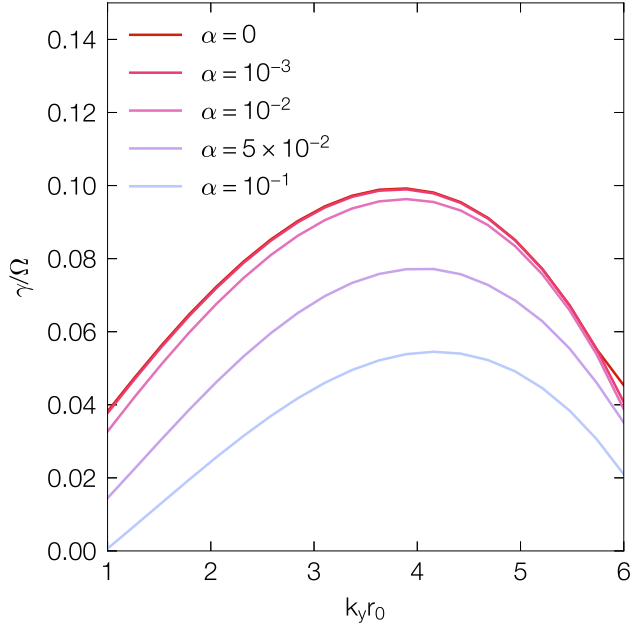


Figure 2. Growth rates of the pure gas RWI for different viscous α values.

framework adopted in this work. Our goal is to reproduce previously reported growth rates for the gas-only RWI to strengthen the reliability of our results. However, no existing study employs exactly the same model setup. For example, LB23 also used a shearing sheet, but their formulation combined gas and dust into a single fluid, complicating direct comparison. Instead, we compare our results with those of Li et al. (2000), who studied the RWI in cylindrical coordinates using an adiabatic equation of state. Specifically, we refer to their homentropic Gaussian bump (HGB) model shown in Figure 10. Using the same parameters, we find slightly lower growth rates, for instance, $\gamma/\Omega = 0.196$ at $m = 4$ and $\gamma/\Omega = 0.188$ at $m = 5$, but the overall trend is consistent.

Then, we compute the growth rates of gas RWI for fiducial parameters chosen in this work, $A = 1.5$ and $w = H$. Figure 2 shows the growth rates for different viscosity strengths. In the absence of viscosity ($\alpha = 0$), it is found that the maximum growth rate peaks at $k_{y,\max}r_0 = 3.89$, and $\gamma_{\max}/\Omega = 0.0989$. The oscillation frequencies ω_r for all modes approach zero, but note that $\omega_r \neq 0$, which means the corotation radius is close to $x = 0$. With the presence of viscosity ($\alpha \neq 0$), the growth rates decrease monotonically for all k_y . However, this decreasing only becomes pronounced for sufficiently strong viscosity ($\alpha \gtrsim 10^{-2}$). For $\alpha = 10^{-1}$, the wavenumber of maximum growth rate

shifts to higher $k_{y,\max}r_0 = 4.16$, and the growth rate drops to $\gamma_{\max}/\Omega = 0.0545$.

4.2. Type I DRWI

Figure 3 shows the DRWI growth rates with the presence of dust. The fiducial parameters are $A = 1.5$, $w = H$ and viscosity $\alpha = 10^{-3}$. We conduct parameter survey on the dust-to-gas density ratios at bump center $\epsilon_{\max} = A_d/A \in [0.1, 0.3, 0.5]$, widths of the dust bump $w_d/H \in [0.05, 0.1, 0.3]^2$, and the Stokes number $St \in [0.001, 0.01, 0.1, 1, 10]$. Two distinct DRWI modes are found (Type I and Type II). Type I modes are dust modified RWI shown as crosses in Figure 3.

For very weak coupling between dust and gas ($St = 10$), the growth rates of Type I modes almost resemble the pure gas RWI results, shown in all panels of Figure 3. This is especially clearly seen in the right column, where dust-to-gas mass ratio, $\epsilon_{\max} = 0.1$, is low in a dust ring. For $St = 1$, the growth rates decrease compared to $St = 10$. However, for smaller Stokes numbers $St < 1$, the growth rates do not drop significantly. Moreover, higher dust-to-gas ratios ϵ_{\max} and wider dust bumps w_d tend to diminish the growth of Type I modes.

In Figure 3, Type I DRWI modes are present across a broad parameter space of ϵ_{\max} , w_d , and St , emerging in all panels. For large dust-to-gas ratios $\epsilon_{\max} = 0.3, 0.5$ and narrow dust rings $w_d/H = 0.05, 0.1$, Type I modes are confined to relatively small azimuthal wavenumbers ($k_y r_0 \leq 5$). This is because that at larger k_y , Type I modes are suppressed, and the Type II modes set in. Notably, Type I and Type II modes never coexist; for a given k_y , only one mode type can emerge, contrary to the findings in LB23 (see §4.7).

Figure 4 shows the eigenfunctions of Type I modes for $\epsilon_{\max} = 0.1$, $w_d/H = 0.3$, and $St = 0.1$ (lower right column of Figure 3). We present the perturbed dust density $\delta\rho_d$, and perturbed vorticity $\delta\zeta$ (defined in Equation (37)), respectively. Dashed vertical lines denote the locations of $x = \pm w_d, \pm 2w_d$ (left column) or $x = \pm w, \pm 2w$ (right column). It is evident that the perturbed vorticity, along with the perturbed gas density (not shown), are confined within the background gas bump, and the perturbed dust density remains within the background dust bump. The perturbed vorticity behaves similarly to the pure gas RWI, exhibiting a pair of counter-propagating Rossby waves across the corotation (see Figure 16 of Ono et al. (2016) and §3.3 of Chang & Youdin (2024)).

² Note that for $\alpha = 10^{-3}$, $w_d/H = 0.05$ more closely matches the numerically computed dust equilibrium profile (see Figure 1).

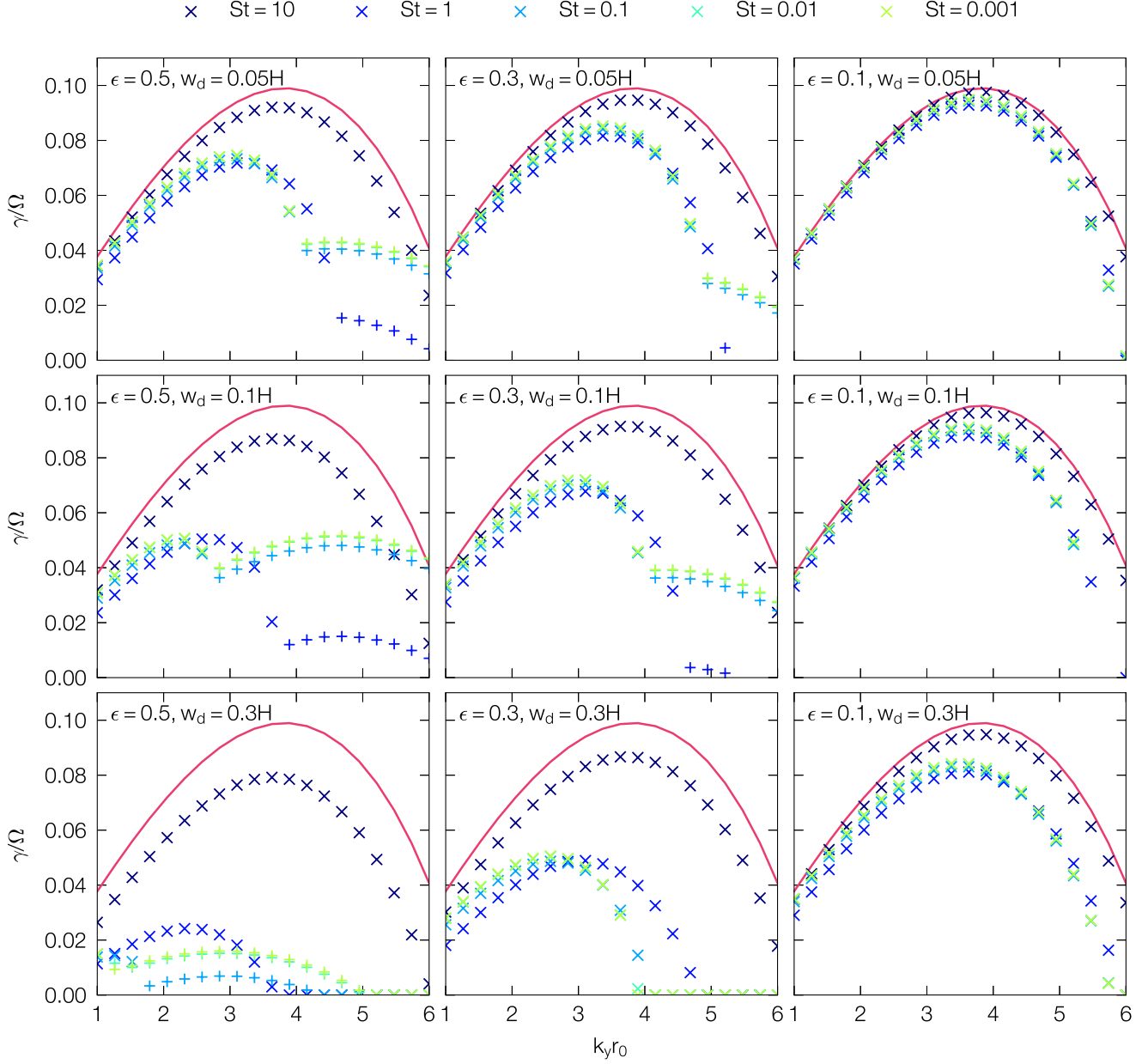


Figure 3. DRWI Growth rates for $\alpha = 10^{-3}$ of different dust-to-gas density ratios at the bump center $\epsilon_{\max} = A_d/A \in [0.5, 0.3, 0.1]$ (from left to right), and different dust bump widths $w_d/H \in [0.05, 0.1, 0.3]$ (from top to bottom). Type I DRWI modes are denoted by crosses, and type II DRWI modes are denoted by plus symbols. Red curves denote pure gas RWI growth rates (§4.1).

4.3. Type II DRWI

Type II DRWI modes are shown as plus symbols in Figure 3. They always appear in pairs. For each pair of modes, they share the same growth rate γ , but possess oppositely-signed oscillation frequencies w_r . Type II modes emerge when dust and gas are well coupled. For $St = 10$, no Type II modes are found in Figure 3. When $St < 1$, the growth rates are generically larger than

$St = 1$ modes. In addition, Type II modes are excited when dust content is high, $\epsilon_{\max} = 0.3, 0.5$, or the width of the dust bump is narrow, $w_d/H = 0.05, 0.1$. Type II modes set in for relatively large azimuthal wavenumbers k_y compared to Type I modes.

Figure 5 shows the eigenfunctions of a pair of Type II modes for $\epsilon_{\max} = 0.5$, $w_d = 0.1$, and $St = 0.1$ (middle left panel of Figure 3). We present the perturbed gas density $\delta\rho_g$, dust density $\delta\rho_d$, gas vortensity δq , and dust

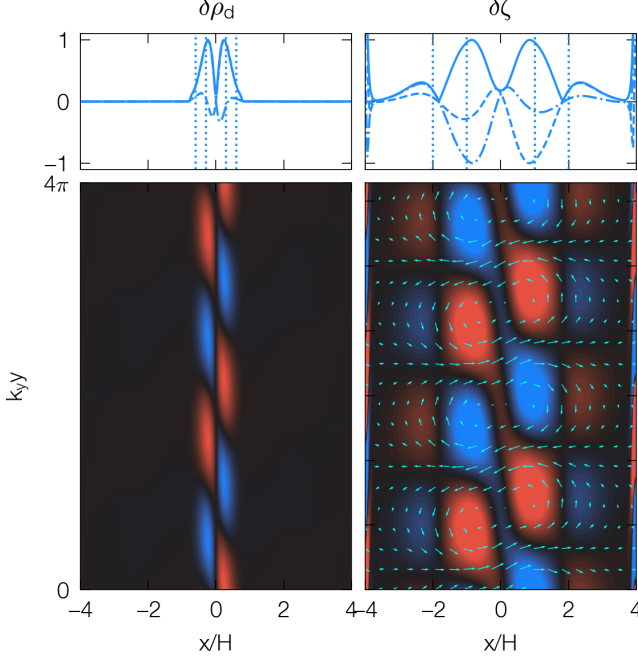


Figure 4. Eigenfunctions of Type I DRWI modes. First row: normalized real (dashed), imaginary (dash-dotted), and absolute (solid) part of the perturbed quantities. Dashed vertical lines denote the locations of $x = \pm w_d, \pm 2w_d$ (left column) or $x = \pm w, \pm 2w$ (right column). Second row: amplitude of perturbed quantities in the (x, y) -plane. Red (blue) denotes positive (negative) values. Arrows denote the perturbed velocity field. Parameters: $A = 1.5$, $w = H$, $\alpha = 10^{-3}$, $k_y r_0 = 3$, $\epsilon_{\max} = 0.1$, $w_d/H = 0.3$, $St = 0.1$, and $\omega/\Omega = 1.3 \times 10^{-5} + 0.081i$.

vortensity δq_d , respectively (see definitions of perturbed vorticities in §4.5). Again, the perturbed gas density is clearly confined by the background gas bump, while the perturbed dust density is confined by the background dust bump. However, unlike Type I modes, the perturbed gas vortensity in this case exhibits a pair of thin waves across $x = 0$, situated between the Rossby waves. The presence of these narrow features serves as an additional signature of Type II modes, complementing their characteristic oppositely signed frequencies.

4.4. Transition of DRWI modes

In Figure 3, we find that at a given k_y , Type I and Type II DRWI modes never coexist. Only one type of mode can be excited for a given k_y . Here, we demonstrate how the two types of modes transition from one to the other. We consider Type I modes as those with corotation radius close to the bump center ($x = 0$), and Type II modes as those two modes share the same growth rate but have oppositely-signed oscillation frequencies. Figure 6 shows the growth rates γ and oscillation fre-

quencies ω_r , for different wavenumbers k_y denoted by different colors. For $k_y r_0 \leq 2$, only one Type I mode is present (plus symbols), with w_r/Ω approaching zero. For $2 < k_y r_0 < 4$, a new Type I mode sets in (crosses). The growth rate of this mode starts from zero and gradually increases with k_y , and the oscillation frequency is different from the first Type I mode, though still close to zero. When two Type I modes show up, we select the one with the higher growth rate for our analysis. At $k_y r_0 = 4$, the two different Type I modes transition to a pair of Type II mode. The corotation radii of Type II modes become far from the bump center with increasing k_y .

4.5. Instability Mechanism

The pure gas RWI mechanism is most clearly reflected in the perturbed vortensity δq . A pair of counter-propagating Rossby waves forms across corotation (Heifetz et al. 1999). This wave pair is shifted in the y -direction, and remains radially symmetric about corotation, consistent with the symmetric potential of the Gaussian bump shown in Figure 1 of Chang & Youdin (2024). The y -direction phase shift causes gas flow passing through the background vorticity minimum ($x = 0$) to primarily enter regions of negative vorticity perturbation, and vorticity maximum to primarily enter regions of positive vorticity perturbation, which is a runaway process (Ono et al. 2016; Chang & Youdin 2024).

The above mechanism can be used to explain the Type I DRWI modes shown in Figure 4. A pair of counter-propagating Rossby waves is located on each side of the corotation. The amplitude of δz is symmetric about x , and the sign is consistent with the arrows and the background vorticity. In contrast, the Type II modes shown in Figure 5 cannot be explained by this mechanism. Specifically, the sign of δq and the direction of the arrows are inconsistent for the thin waves, suggesting that advection alone does not dominate the driving mechanism of Type II modes.

To clarify the physical mechanism of the Type I and Type II modes, we analyze the source of the perturbed gas and dust vorticities. We derive the vortensity equation in Appendix C. The gas vorticity ζ and vortensity q in our shearing sheet model are defined as

$$\zeta = (\nabla \times \mathbf{v}_g)_z, \quad (35)$$

$$q = (2\Omega + \zeta)/\rho_g, \quad (36)$$

and the corresponding perturbed quantities are

$$\delta \zeta = (\nabla \times \delta \mathbf{v}_g)_z, \quad (37)$$

$$\delta q = \delta \zeta / \rho_{g0} - (2\Omega + \zeta) \delta \rho_g / \rho_{g0}^2. \quad (38)$$

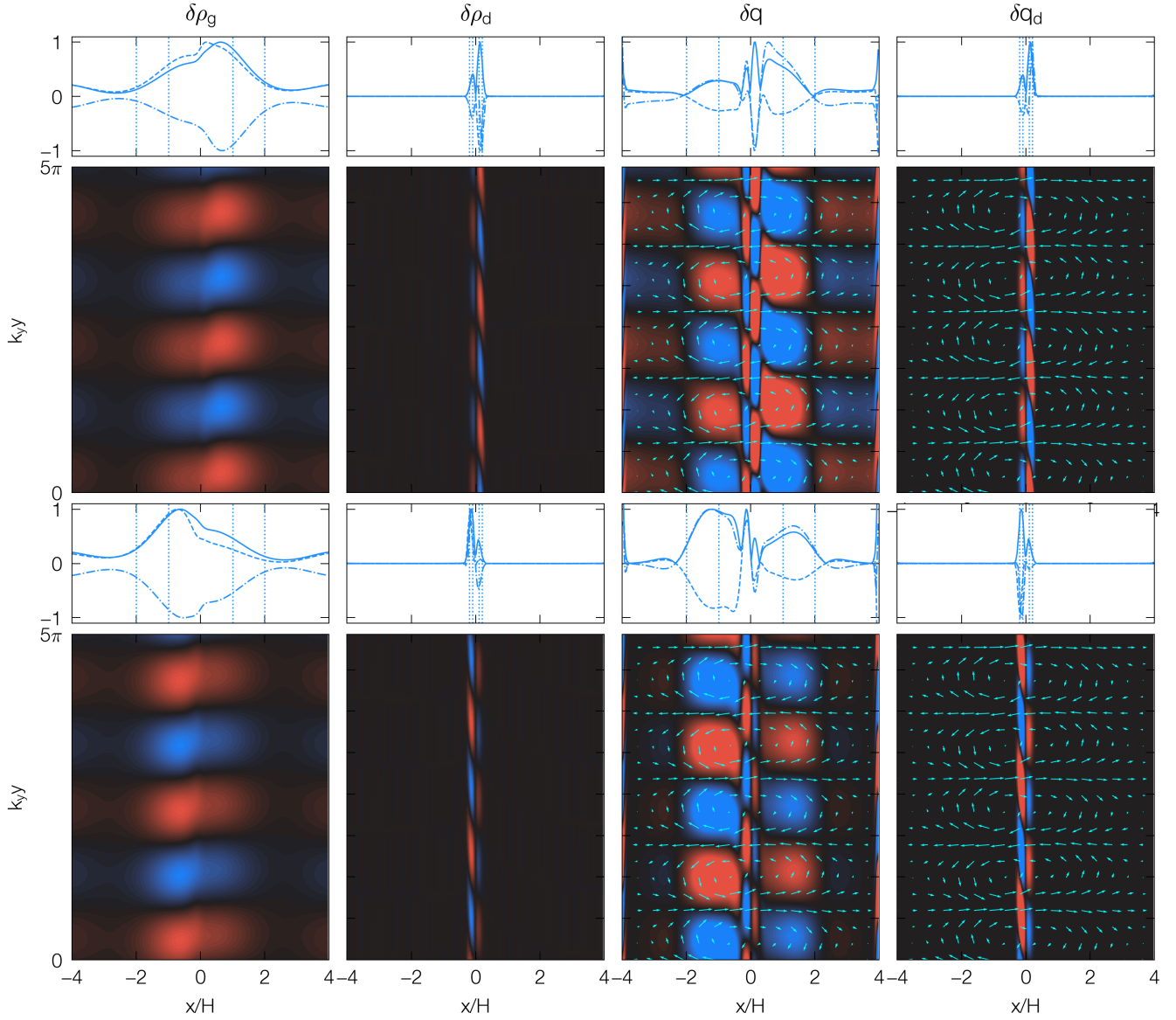


Figure 5. Eigenfunctions of a pair of Type II DRWI modes. Top rows (right mode): $A = 1.5$, $w = H$, $\alpha = 10^{-3}$, $k_y r_0 = 5$, $\epsilon_{\max} = 0.5$, $w_d/H = 0.1$, $St = 0.01$, and $\omega/\Omega = -0.0955 + 0.047i$. Bottom rows (left mode): $\omega/\Omega = 0.0955 + 0.047i$.

Appendix C gives the vortensity equation,

$$\frac{Dq}{Dt} = \frac{S}{\rho_g}, \quad (39)$$

and the perturbed vortensity equation

$$(-i\omega + ik_y v_{gy0})\delta q + \delta v_{gx} \frac{\partial q_0}{\partial x} \approx S'_{\text{drag}}, \quad (40)$$

where

$$S'_{\text{drag}} = \frac{1}{\rho_g} \frac{\epsilon}{t_s} \nabla \times (\delta \mathbf{v}_d - \delta \mathbf{v}_g). \quad (41)$$

Figure 7 shows the perturbed gas vortensity δq , advection term $s'_{\text{adv}} = -\delta v_{gx}(\partial q_0/\partial x)/(-i\omega + ik_y v_{gy0})$, and

drag force term $s'_{\text{drag}} = S'_{\text{drag}}/(-i\omega + ik_y v_{gy0})$ in $(x-y)$ plane. The top panels of Figures 9 and 10 show the same quantities at $y = 0$. For the Type I mode, a pair of classic Rossby waves dominates the perturbed vortensity. The advection term is the major contribution to the perturbed vortensity, consistent with the instability mechanism of the pure gas RWI. In Figure 9, the drag force term exhibits an opposite sign relative to δq for one of the Rossby waves, indicating that dust acts to damp the Type I DRWI modes.

The right column of Figure 7 shows the left mode of a pair of Type II modes, presented in Figure 5. In addition to the classic Rossby waves, a pair of thin waves

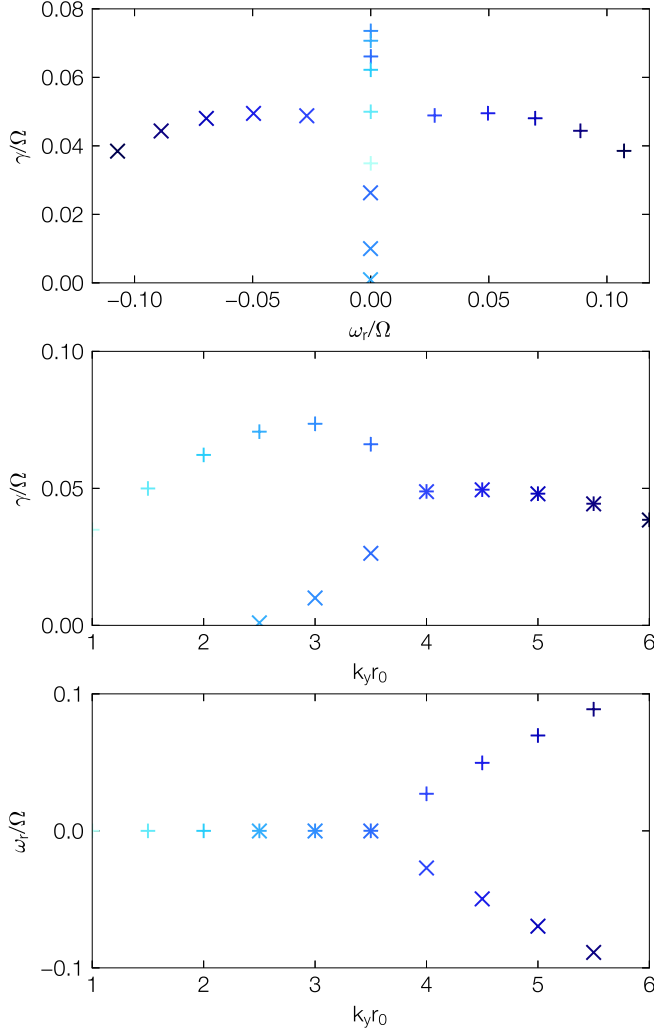


Figure 6. Growth rates γ and oscillation frequencies ω_r for different wavenumbers k_y . Parameters: $A = 1.57$, $w = H$, $\alpha = 10^{-3}$, $\epsilon_{\max} = 0.3$, $w_d = 0.1$, and $St = 0.01$.

is present between the classic waves, which is the key distinction from Type I modes. The advection term drives the classic Rossby waves, while the drag force term serves as the underlying source of the thin waves. The amplitude of the perturbed vortensity δq of the thin waves is comparable to that of the classic Rossby waves. In Figure 10, the drag force term has the same sign as δq , which acts to promote the Type II modes.

We also analyze the dust vortensity budget. The perturbed dust vortensity equation is (Appendix C)

$$(-i\omega + ik_y v_{dy0})\delta q_d + \delta v_{dx} \frac{\partial q_{d0}}{\partial x} \approx S'_{d,\text{drag}}, \quad (42)$$

where the drag force term dominates over the dust diffusion term for S'_d . The perturbed dust vortensity driven

by the drag force is expressed by

$$S'_{d,\text{drag}} = -\frac{1}{\rho_d t_s} \nabla \times (\delta \mathbf{v}_d - \delta \mathbf{v}_g). \quad (43)$$

Figure 8 shows the dust perturbed vortensity δq_d , advection term $s'_{d,\text{adv}} = -\delta v_{dx}(\partial q_{d0}/\partial x)/(-i\omega + ik_y v_{dy0})$, and drag force term $s'_{d,\text{drag}} = S'_{d,\text{drag}}/(-i\omega + ik_y v_{dy0})$ in $(x-y)$ plane. For both Type I and Type II modes, a pair of thin waves, corresponding to the background dust width, emerge on both sides of the corotation radius. The advection term is clearly the dominant contributor to the perturbed dust vortensity in both cases. This contrasts with the perturbed gas vortensity shown in Figure 7, where the drag force serves as the source of thin waves.

4.6. Parameter Study

We perform parameter study on the growth rates of Type I and Type II DRWI. The free parameters in the linear analysis include the gas bump amplitude A , gas bump width w , dust bump amplitude A_d , dust bump width w_d , Stokes number St , and viscosity α . The parameter ranges are chosen to be gas bump amplitude $A \in [1.2, 3.8]$, dust bump amplitude $A_d/A = \{0.1, 0.3\}$, gas bump width $w/H = \{1, 1.2, 1.5\}$, and dust bump width $w_d/H = \{0.1, 0.3\}$. The Stokes numbers are taken to be $St = \{0.01, 0.1\}$. The viscous parameter is set to $\alpha = \{10^{-4}, 5 \times 10^{-4}\}$, consistent with both theoretical predictions and observational data (Flaherty et al. 2017, 2018, 2020; Lesur et al. 2023). Figures 11-14 show the growth rates across our parameter space.

For Type I modes, the growth rates decrease monotonically with A_d and w_d (Figure 3, Figures 11-14). When varying the gas bump parameters, the growth rates increase with A but drop significantly with w . Notably, when $A_d/A = 0.3$, a slight increase in w/H from 1 to 1.2 can completely suppress the Type I modes. These trends can be explained by the impact of drag force on the perturbed vortensity. In Figure 9, we see that larger values of A_d , w_d , and w , or smaller values of A , result in a greater suppression of δq in the inner part of the classic Rossby waves, due to the drag force term (solid red).

For Type II modes, the growth rates increase monotonically with A_d , in contrast to Type I modes (Figure 3, Figures 11-14). The growth rates do not vary monotonically with w_d , as shown in Figure 3, where maxima occur at $w_d = 0.1$ but vanish at $w_d = 0.3$. When varying the gas bump parameters, the growth rates increase with A , but decrease with w , similar to Type I modes. These trends can also be attributed to the effect of drag force term on the perturbed vortensity. Type II modes rely

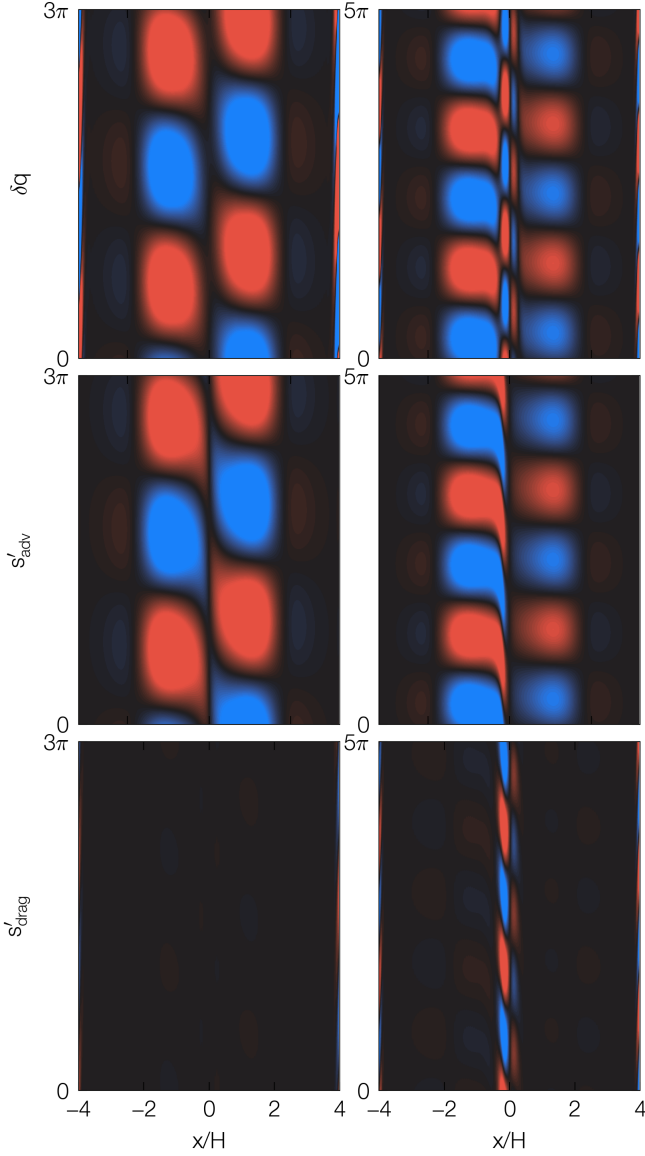


Figure 7. Terms in the perturbed vortensity equation (40) shown in $(x/H - k_y y)$ plane. Left column: Type I mode in Figure 4. Right column: Type II mode in Figure 5 (left mode). Top to bottom row: perturbed vortensity δq , advection term, and drag force term. All panels in each column have the same colorbar range.

on the presence of thin waves in the perturbed vortensity. In Figure 10, smaller values of A_d and A , or larger values of w_d and w , result in weaker thin Rossby waves due to the drag force term (solid red).

Moreover, the growth rates show a slight increase with larger α for Type I modes. The underlying reason for this trend is not yet fully understood and warrants further investigation in future work. The Stokes numbers of $St = 0.01$ and $St = 0.1$ do not produce significant

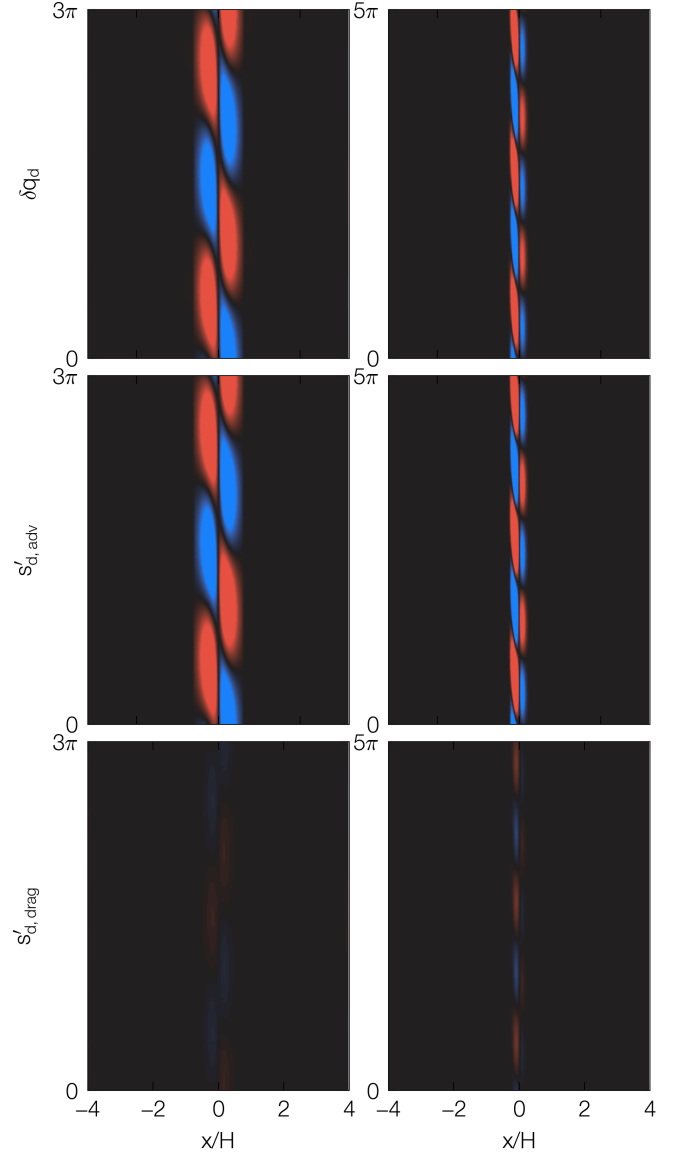


Figure 8. Same to Figure 7 but with terms in the perturbed dust vortensity equation (42).

differences in growth rates of Type I modes, consistent with the results shown in Figure 3. The growth rates decrease with α for Type II modes. The Stokes number of $St = 0.01$ gives rise to slightly stronger growth rates than $St = 0.1$, as Type II modes prefer stronger coupling between gas and dust.

Local numerical simulations revealed that the non-linear evolution of Type II modes can yield ring-like substructures, whereas Type I modes gave rise to vortices (LB23). Thus, we search the parameter space where Type II growth rates are greater than Type I. When $A_d/A = 0.3$ (Figures 11 and 12), Type II modes tend to dominate generically for w/H greater than unity, be-

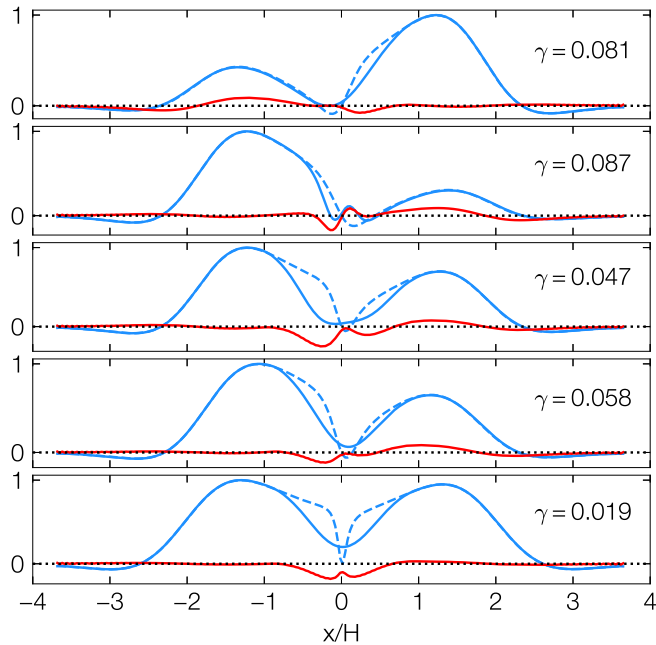


Figure 9. Real part of δq (solid blue), advection term s'_{adv} (dashed blue), and drag force term s'_{drag} (red) at $y = 0$, normalized by the maximum of real δq . Top panel: Type I mode in Figure 7, with $A = 1.5$, $w = H$, $\epsilon_{\text{max}} = 0.1$, $w_d = 0.3$. Lower panels have almost identical parameters, but with one parameter changed in each. Specifically, the changes are $w_d = 0.1$, $\epsilon_{\text{max}} = 0.3$, $A = 1.2$, and $w/H = 1.1$, from top to bottom, respectively.

cause Type I modes are suppressed. When $A_d/A = 0.1$ (Figures 13 and 14), Type I modes dominate in most cases because the dust content is low. Type II modes only take over for w/H greater than unity and small A when $w_d/H = 0.1$. When $w_d/H = 0.3$, most of the Type II modes vanish.

4.7. Comparison to LB23

LB23 were the first to identify DRWI via linear theory and shearing box numerical simulations. Although all terms in the conservation laws of equations (1)-(4) are identical between their work and ours, they used single-fluid formulation to conduct linear analysis, combining dust and gas equations (Lin & Youdin 2017). In contrast, we adopt the two-fluid equations, as applied in the linear analysis of streaming instability (Youdin & Goodman 2005), where dust and gas are treated as separate fluids. As a result, there are a number of similarities and differences between our work and theirs. For clarity, we highlight the key points below.

First, we discuss the similarities. Both works identify two distinct DRWI modes (Type I and II). This is achieved by setting the equilibrium radial velocities

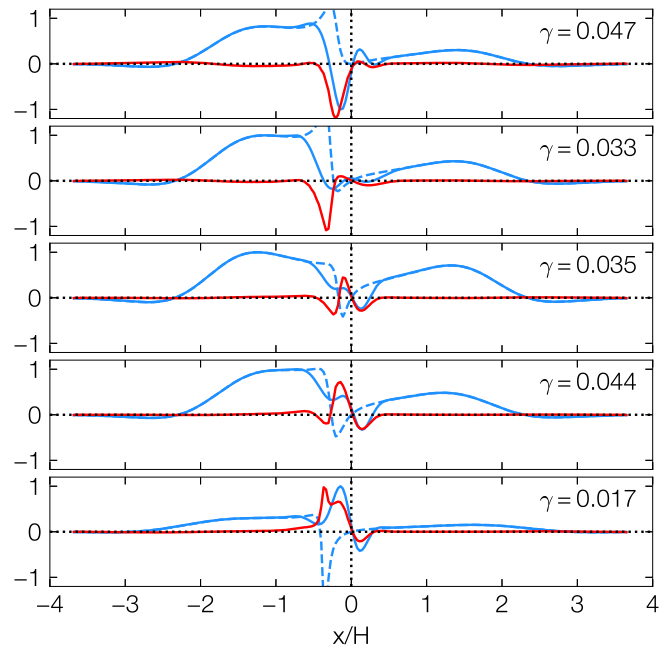


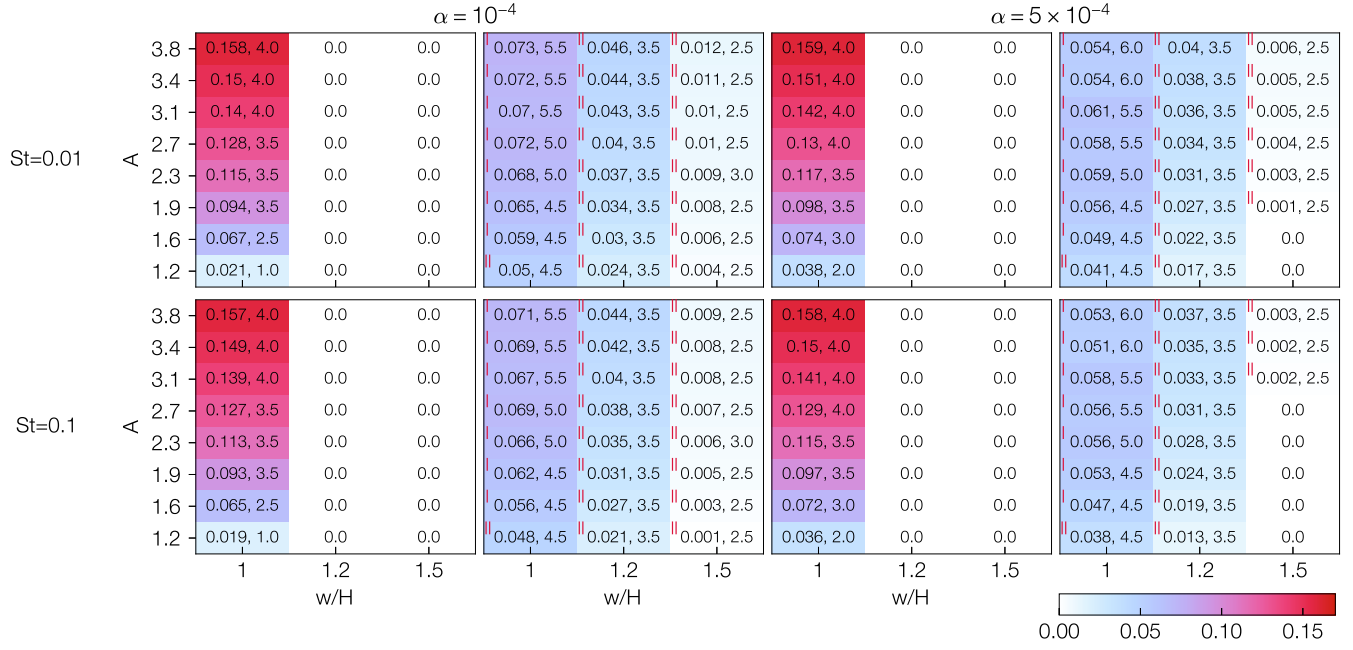
Figure 10. Same as Figure 9 but for Type II modes. Top panel: Type II mode in Figure 7, with $A = 1.5$, $w = H$, $\epsilon_{\text{max}} = 0.5$, $w_d = 0.1$. Lower panels have almost identical parameters, but with one parameter changed in each. Specifically, the changes are $w_d = 0.2$, $\epsilon_{\text{max}} = 0.3$, $A = 1.2$, and $w/H = 1.2$, from top to bottom, respectively.

to zero, either for the single-fluid model in LB23 or for the dust and gas components in this work, which effectively filters out the streaming instability. Type I modes are closely related to the pure gas RWI, whereas Type II modes arise from dust-gas coupling. Additionally, the oscillation frequencies w_r of Type I modes approach zero (but not equal to), while those of Type II modes are generally greater. For Type I modes, the perturbed vortensity is primarily driven by the advection of background vortensity, whereas for Type II modes (thin waves), the perturbation is driven by dust-gas drag (baroclinic term in LB23 as they combined the two-fluid equations).

The major distinction between this work and LB23 lies in the behavior of the two types of DRWI modes. LB23 found that both modes can coexist for a given k_y (see their Appendix D), whereas our results indicate that for a given k_y , only one mode grows at a time. However, as k_y varies, our results suggest that a transition between the two types of modes can occur. The underlying cause of this discrepancy remains unclear. Future studies could further investigate this issue, possibly by exploring alternative dust diffusion models and comparing the results.

5. DRWI IN ALMA RINGS

$$A_d/A = 0.3; w_d/H = 0.1$$



$$A_d/A = 0.3; w_d/H = 0.3$$

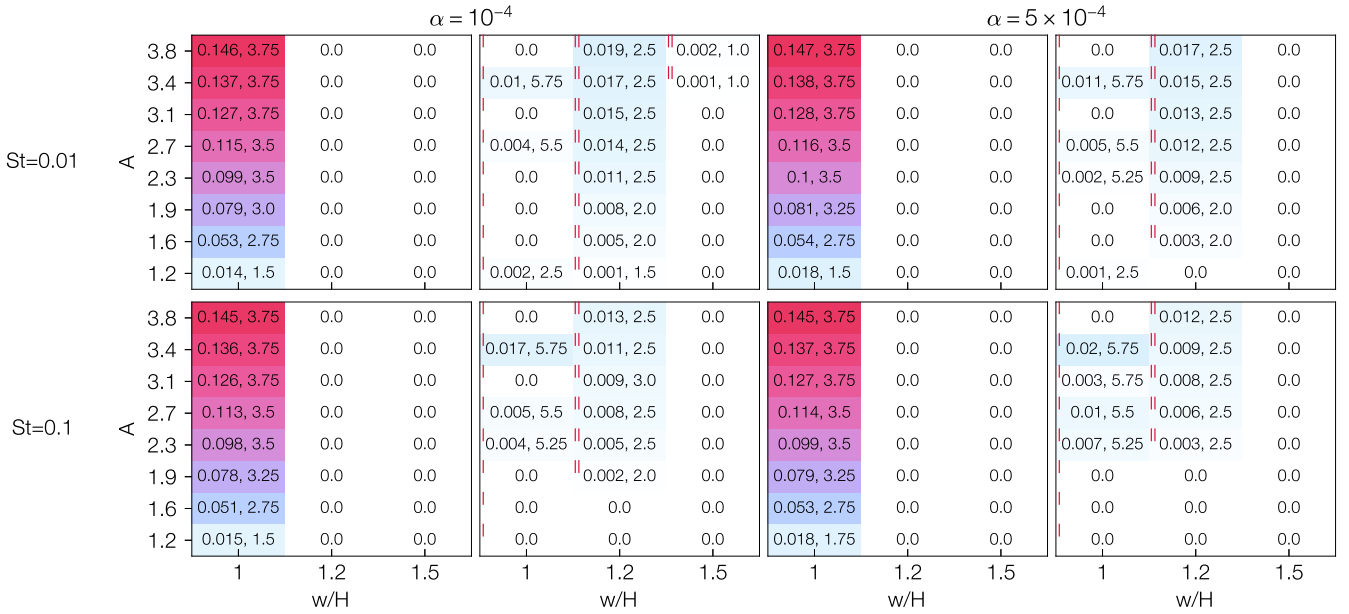


Figure 12. Same as Figure 11 with $A_d/A = 0.3$ and $w_d/H = 0.3$.

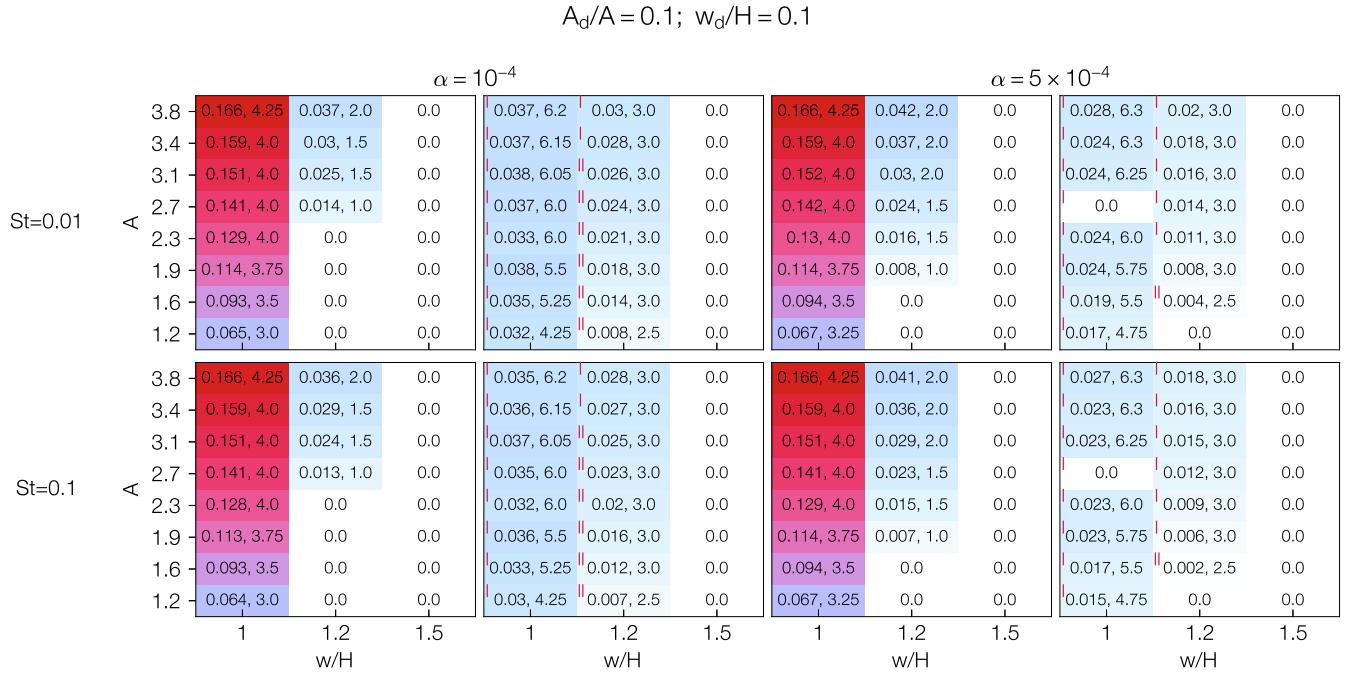


Figure 13. Same as Figure 11 with $A_d/A = 0.1$ and $w_d/H = 0.1$.

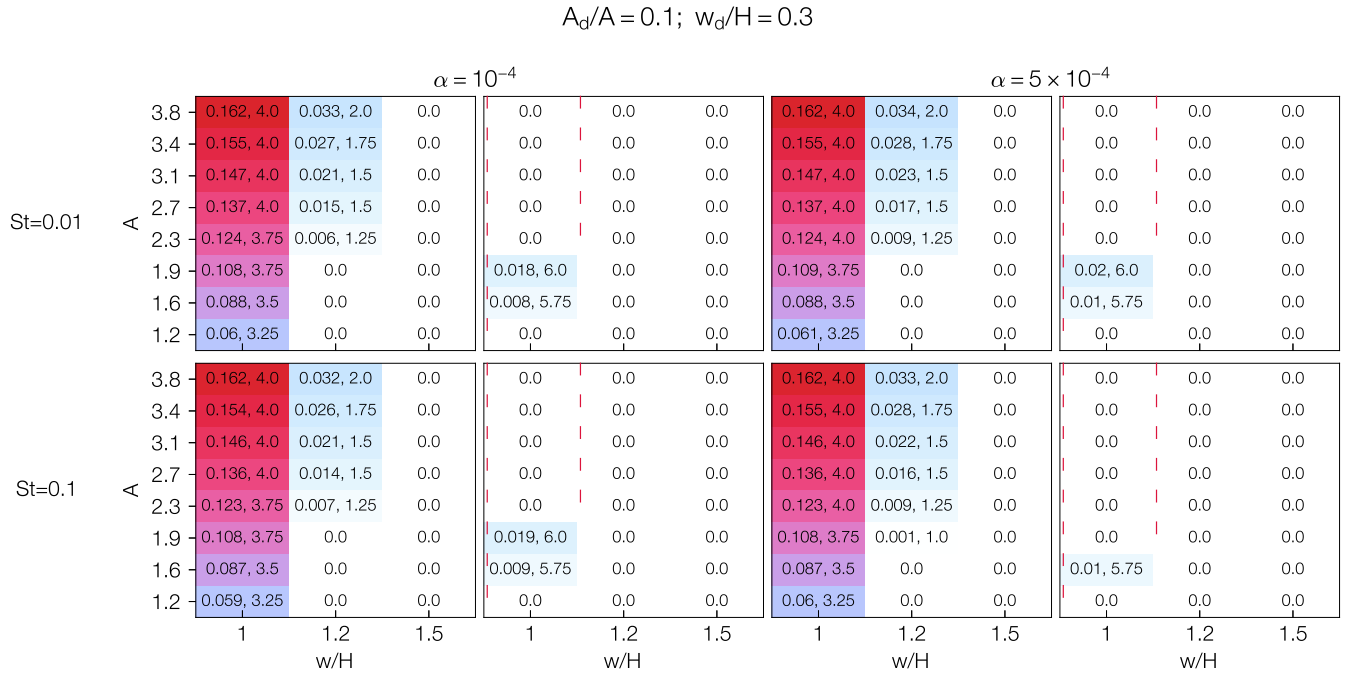


Figure 14. Same as Figure 11 with $A_d/A = 0.1$ and $w_d/H = 0.3$.

We investigate the onset of DRWI within the parameter space spanned by ALMA rings of DSHARP sources. In the following subsections, we discuss the bump parameters constrained by observations (§5.1), the presence of DRWI and its implication to dust growth in rings (§5.2).

This paper focuses on the linear behavior of the DRWI. However, the linear phase is usually transient, and to facilitate direct comparison with ALMA rings, it is essential to examine the nonlinear evolution of the instability. Local shearing-box simulations on (radial) H -scales have shown that Type II modes can yield ring-like substructures, while Type I modes tend to produce vortices (LB23). Given the tendency of Type I modes to generate non-axisymmetric features, we expect most ALMA rings to be stable or only marginally unstable to Type I DRWI. This expectation is consistent with our findings for the DSHARP sources. On the other hand, ring-like structures persist under Type II DRWI in local simulations. Whether these structures can survive in global simulations remains an open question, and future numerical studies are needed to explore this further. Detailed discussions follow below.

5.1. Gaussian Bump Parameters

The dust and gas bump parameters, w_d, w, A_d, A , can be either observationally constrained, thanks to the DSHARP Programme (Andrews et al. 2018, D+18), or approximated by numerical simulations of planet-disk interactions. We detail the values chosen below.

D+18 selected a sample of sufficiently face-on DSHARP sources, which possess radially well separated, high-contrast dust rings. The dust bump width w_d is directly obtained by fitting a Gaussian profile to the observed ring emission. D+18 employed a Gaussian function similar to our Eq. (10), but without the density floor that applied far from the bump center. Their fittings gave w_d/H for eight rings, listed in Table 1. The gas bump width w is constrained by D+18 as well. A lower limit is set by $w_{\min} = w_d$, and an upper limit w_{\max} is set by the separation of the ring and the nearest intensity minimum. Rosotti et al. (2020) further estimated gas bump width w_{rot} by extracting the gas rotation curve from the emission lines, for four rings in HD 163296 and AS 209, listed in Table 1.

Moreover, the dust bump amplitude A_d can also be directly obtained from the Gaussian fitting of intensity. The dust density amplitude derived from deconvolved dust intensity is listed in Table 1, using eq. 7 in D+18 for which thermal emission is assumed optically thin.

To estimate the gas bump amplitude A , constraints shall be placed on the dust-to-gas density ratio Σ_d/Σ_g

at the ring center. D+18 estimated the dust surface density Σ_d by assuming optically thin thermal emission. They further place an upper limit on the gas surface density $\Sigma_{g,\text{max}}$ by demanding the disk to be gravitationally stable (Toomre $Q > 2$; Toomre (1964)). Unfortunately, this upper limit can only give a lower limit on dust-to-gas mass ratio ~ 0.01 . We then opt for determine Σ_d/Σ_g from numerical simulations, using those with planets carving gaps and rings. These simulations found Σ_d/Σ_g between a few times of 0.01 and 0.1 (e.g. Paardekooper & Mellema 2004; Pinilla et al. 2012; Drążkowska et al. 2019). Thus, we take $\Sigma_d/\Sigma_g = A_d/A = 0.1$ at the bump center.

Note that the unstratified shearing box employed throughout this work is applicable to the midplane of the disk, where vertical gravity is nearly negligible. Above, we use surface densities to determine the dust-to-gas ratio, which is justified since both gas and dust in protoplanetary disks typically follow Gaussian distributions vertically, with mass densities peaking at the midplane.

The Stokes number is chosen to be $\text{St} = 10^{-3}$, as observational constraints suggest it typically ranges from 10^{-3} to 10^{-2} (D+18, Rosotti et al. 2020). In Figure 3, we find that $\text{St} = 10^{-3}$ and $\text{St} = 10^{-2}$ produce similar growth rates. The viscosity is selected to be relatively low, with $\alpha = 10^{-4}$ (Flaherty et al. 2017, 2018, 2020; Rosotti et al. 2020).

5.2. Excitation of DRWI in Rings

It is found that while Type I modes can be triggered for w_{\min} in some rings, they do not emerge for w_{\max} . When the rotation curve provides a measurement of w_{rot} , only one out of four rings meets the conditions for the onset of Type I mode. Local numerical simulations by LB23 showed that the non-linear stage of Type I modes can lead to azimuthal clumps, similar to the pure gas RWI. The absence of Type I modes in many ALMA rings listed in Table 1 suggests that only a limited number of pressure bumps shaped by annular substructures are capable of inducing azimuthal asymmetries. This is in alignment with the ALMA observations, which have showed that only around 10% of the ringed disks exhibit crescent-like azimuthal asymmetries (Huang et al. 2018a).

Type II modes are completely absent in all eight rings, as the dust bump width w_d is too large to excite these modes. Taking Ring 1 (B74) of AS 209 as an example, w_d/H needs to be as small as 0.1 or lower to excite the Type II DRWI using w_{rot} . However, it could be that narrower rings are too thin to be observed by ALMA. For example, Jennings et al. (2022) applied the super-resolution code FRANK to 20 DSHARP sources (Jen-

Table 1. Parameters for Rings in DSHARP Sources.

Source (1)	Ring (2)	Name (3)	A_d (4)	w_d/H (5)	w_{\min}/H (6)	w_{\max}/H (7)	w_{rot}/H (8)
AS 209	1	B74	0.19	0.6	1	3.5	1.4
AS 209	2	B120	0.2	0.4	1	2	1
Elias 24	1	B77	0.17	0.6	1	2	/
HD 163296	1	B67	0.19	1.6	1.6	3	3.3
HD 163296	2	B100	0.14	0.7	1	2	3.5
GW Lup	1	B85	0.13	0.6	1	1.25	/
HD 143006	1	B41	0.1	1.9	1.9	5	/
HD 143006	2	B65	0.09	2	2	2.7	/
Fiducial			A (9)		w/H (10)	α (11)	
			1.5		1	10^{-3}	

Note. (1) Subsample of DSHARP sources. (2) Internal numbering of rings in D+18. (3) Ring name from Huang et al. (2018a). (4) Dust bump amplitude. (5) Dust bump width. (6) Minimum gas bump width. (7) Maximum gas bump width. (8) Gas bump width by rotation curve. (9) Fiducial gas bump amplitude (§4). (10) Fiducial gas bump width. (11) Fiducial viscous α value. See §5.1 for more detailed explanation.

Table 2. Excitation of DRWI at $\text{St} = 10^{-3}$, $\alpha = 10^{-4}$ and $k_y \in [1, 7]$.

Source (1)	Ring (2)	Name (3)	A_d/A (4)	Type I; Type II (5)	Type I; Type II (6)	Type I; Type II (7)
				w_{\min}	w_{\max}	w_{rot}
AS 209	1	B74	0.1	Y; N	N; N	N; N
AS 209	2	B120	0.1	Y; N	N; N	Y; N
Elias 24	1	B77	0.1	Y; N	N; N	/
HD 163296	1	B67	0.1	N; N	N; N	N; N
HD 163296	2	B100	0.1	Y; N	N; N	N; N
GW Lup	1	B85	0.1	Y; N	N; N	/
HD 143006	1	B41	0.1	N; N	N; N	/
HD 143006	2	B65	0.1	N; N	N; N	/

Note. (1), (2) and (3) are same as Table 1. (4) dust-to-gas ratio at bump center $\epsilon_{\max} = A_d/A$. (5) onset of DRWI modes (Type I and II) for w_{\min} in Table 1. (6) onset of DRWI modes for w_{\max} in Table 1. (7) onset of DRWI modes for w_{rot} in Table 1.

nings et al. 2020) and found that high-contrast rings are brighter and on average 26% narrower. Hence, the measurements of ring widths of DSHARP sources should be treated as upper limits due to the limited spatial resolution. Moreover, the intrinsic dust ring widths can be different from the observed values, due to the optically thin assumption made in D+18. The intrinsic optical depth might be greater as small dust species can contribute a large fraction of opacity at mm band, and the emission becomes optically thick. This can lead to the observed rings looking wider at ALMA band. The coagulation-fragmentation processes can modify the dust size distribution within the ring, and may further enhance the optical depth (Yang et al. 2025). This enhancement

could make the observed rings even wider. If many rings are intrinsically considerably narrower compared to DSHARP observations, Type II DRWI may still be plausible to operate.

Shearing box simulations by LB23 demonstrated that Type II modes can lead to the persistence of rings and the formation of small gravitationally bound clumps in the nonlinear stage. However, these simulations were performed on extremely narrow radial domains (on H -scales), limiting their applicability to global disk structures. Larger-scale two-fluid simulations have been carried out in the context of a Neptune-mass planet carving rings (Chan & Paardekooper 2024), but this study did not directly compare their results with the

linear theory of DRWI. Future global simulations with high spatial resolution are needed to validate or revise the conclusions drawn from shearing box simulations.

Another possibility is that the observed rings are already the outcome of the nonlinear evolution of Type II modes. If so, this would suggest that while Type II modes can support the persistence of rings, they are not efficient at triggering Type I modes and producing azimuthal asymmetries.

Finally, it is also possible that Type II DRWI is absent in many observed rings, implying that additional physical processes may be required to promote dust growth and planetesimal formation in annular substructures. A companion paper in this series investigates the linear behavior of the global SI in the presence of a pressure bump. The key question is whether SI can operate within a pressure bump and how its growth depends on bump parameters in both the linear and nonlinear regimes.

6. CONCLUSIONS

In this paper, we investigate the linear properties of the DRWI in the presence of a radial pressure bump, representing annular substructures in protoplanetary disks. To this end, we perform a linear analysis of the two-fluid dust-gas equations, setting the background radial velocities to zero to suppress the SI. The spectral code DEDALUS is employed to solve the eigenvalue problem. Our main findings are summarized below:

1. Two types of DRWI modes are identified: Type I modes, which are dust-modified versions of the classic gas RWI, and Type II modes, which arise from dust-gas coupling. This confirms the findings of LB23, who used a single-fluid formulation for dust and gas.
2. Type I and Type II modes never coexist for a given k_y . Typically, Type I modes dominate at lower k_y , while Type II modes emerge at higher k_y . A transition between the two occurs as k_y varies.
3. The instability mechanism of Type I modes is driven by the advection of background vorticity into perturbed vorticity. Type II modes consist of two main waves: the classic Rossby waves, which are advection-driven, and the thin waves, which are driven by dust-gas drag.

4. The growth rates of Type I (Type II) modes decrease (increase) with dust-to-gas ratio ϵ_{\max} (or equivalently, A_d). For both types, the growth rates are enhanced by increasing A or decreasing w .
5. Applying bump parameters constrained from ALMA rings (DSHARP sources), we find that Type I modes can emerge in one out of four rings, potentially explaining the general absence of azimuthal asymmetries in many ALMA disks.
6. Type II modes are absent in all eight ALMA rings. However, it remains an open question whether narrower rings, capable of triggering Type II DRWI, are more common in protoplanetary disks but remain unresolved by ALMA, or ALMA rings appear artificially widened due to optical depth effects. Alternatively, the absence of Type II DRWI in these systems may be genuine, suggesting that additional mechanisms are needed to promote dust growth and planetesimal formation within annular substructures.

ACKNOWLEDGEMENTS

We thank our referee, Henrik Latter, for the detailed comments that improved the clarity of this manuscript. We thank Hanpu Liu and Lile Wang for the fruitful discussions. CC acknowledges funding from NSERC Canada and Nanjing University. YPL is supported in part by the Natural Science Foundation of China (grants 12373070 and 12192223), the Natural Science Foundation of Shanghai (grant NO. 23ZR1473700). ZX acknowledges funding from the Carlsberg Foundation (Semper Ardens: Advance grant FIRSTATMO). RL acknowledges support from the Heising-Simons Foundation 51 Pegasi b Fellowship. CY is supported by the National SKA Program of China (grant 2022SKA0120101) and the National Natural Science Foundation of China (grants 11873103 and 12373071). MKL is supported by the National Science and Technology Council (grants 112-2112-M-001-064-, 113-2124-M-002-003-) and an Academia Sinica Career Development Award (AS-CDA-110-M06).

DATA AVAILABILITY

The data underlying this article will be shared on reasonable request to the corresponding author.

REFERENCES

- Andrews, S. M. 2020, *ARA&A*, 58, 483, doi: [10.1146/annurev-astro-031220-010302](https://doi.org/10.1146/annurev-astro-031220-010302)
- Andrews, S. M., Huang, J., Pérez, L. M., et al. 2018, *ApJL*, 869, L41, doi: [10.3847/2041-8213/aaf741](https://doi.org/10.3847/2041-8213/aaf741)

- Bae, J., Isella, A., Zhu, Z., et al. 2023, in *Astronomical Society of the Pacific Conference Series*, Vol. 534, *Protostars and Planets VII*, ed. S. Inutsuka, Y. Aikawa, T. Muto, K. Tomida, & M. Tamura, 423, doi: [10.48550/arXiv.2210.13314](https://doi.org/10.48550/arXiv.2210.13314)
- Bai, X.-N., & Stone, J. M. 2010, *ApJ*, 722, 1437, doi: [10.1088/0004-637X/722/2/1437](https://doi.org/10.1088/0004-637X/722/2/1437)
- . 2014, *ApJ*, 796, 31, doi: [10.1088/0004-637X/796/1/31](https://doi.org/10.1088/0004-637X/796/1/31)
- Barge, P., & Sommeria, J. 1995, *A&A*, 295, L1. <https://arxiv.org/abs/astro-ph/9501050>
- Binkert, F. 2023, *MNRAS*, 525, 4299, doi: [10.1093/mnras/stad2471](https://doi.org/10.1093/mnras/stad2471)
- Birnstiel, T. 2024, *ARA&A*, 62, 157, doi: [10.1146/annurev-astro-071221-052705](https://doi.org/10.1146/annurev-astro-071221-052705)
- Birnstiel, T., Dullemond, C. P., & Brauer, F. 2010, *A&A*, 513, A79, doi: [10.1051/0004-6361/200913731](https://doi.org/10.1051/0004-6361/200913731)
- Blum, J. 2018, *SSRv*, 214, 52, doi: [10.1007/s11214-018-0486-5](https://doi.org/10.1007/s11214-018-0486-5)
- Blum, J., & Wurm, G. 2008, *ARA&A*, 46, 21, doi: [10.1146/annurev.astro.46.060407.145152](https://doi.org/10.1146/annurev.astro.46.060407.145152)
- Boyd, J. 2001, *Chebyshev and Fourier Spectral Methods: Second Revised Edition*, Dover Books on Mathematics (Dover Publications). <https://books.google.com/books?id=lEWnQWyzLQYC>
- Burns, K. J., Vasil, G. M., Oishi, J. S., Lecoanet, D., & Brown, B. P. 2020, *Physical Review Research*, 2, 023068, doi: [10.1103/PhysRevResearch.2.023068](https://doi.org/10.1103/PhysRevResearch.2.023068)
- Carrera, D., Johansen, A., & Davies, M. B. 2015, *A&A*, 579, A43, doi: [10.1051/0004-6361/201425120](https://doi.org/10.1051/0004-6361/201425120)
- Chan, K., & Paardekooper, S.-J. 2024, *MNRAS*, 528, 5904, doi: [10.1093/mnras/stae089](https://doi.org/10.1093/mnras/stae089)
- Chang, E., & Youdin, A. N. 2024, *arXiv e-prints*, arXiv:2407.12722, doi: [10.48550/arXiv.2407.12722](https://doi.org/10.48550/arXiv.2407.12722)
- Chen, K., & Lin, M.-K. 2020, *ApJ*, 891, 132, doi: [10.3847/1538-4357/ab76ca](https://doi.org/10.3847/1538-4357/ab76ca)
- Cimerman, N. P., & Rafikov, R. R. 2023, *MNRAS*, 519, 208, doi: [10.1093/mnras/stac3507](https://doi.org/10.1093/mnras/stac3507)
- Cui, C., & Bai, X.-N. 2021, *MNRAS*, 507, 1106, doi: [10.1093/mnras/stab2220](https://doi.org/10.1093/mnras/stab2220)
- . 2022, *MNRAS*, 516, 4660, doi: [10.1093/mnras/stac2580](https://doi.org/10.1093/mnras/stac2580)
- Cui, C., & Lin, M.-K. 2021, *MNRAS*, 505, 2983, doi: [10.1093/mnras/stab1511](https://doi.org/10.1093/mnras/stab1511)
- Cui, C., Tripathi, A., Yu, C., Lin, M.-K., & Youdin, A. 2024, *arXiv e-prints*, arXiv:2407.02103, doi: [10.48550/arXiv.2407.02103](https://doi.org/10.48550/arXiv.2407.02103)
- Dong, R., Zhu, Z., & Whitney, B. 2015, *ApJ*, 809, 93, doi: [10.1088/0004-637X/809/1/93](https://doi.org/10.1088/0004-637X/809/1/93)
- Drażkowska, J., Li, S., Birnstiel, T., Stammer, S. M., & Li, H. 2019, *ApJ*, 885, 91, doi: [10.3847/1538-4357/ab46b7](https://doi.org/10.3847/1538-4357/ab46b7)
- Drażkowska, J., Bitsch, B., Lambrechts, M., et al. 2023, in *Astronomical Society of the Pacific Conference Series*, Vol. 534, *Protostars and Planets VII*, ed. S. Inutsuka, Y. Aikawa, T. Muto, K. Tomida, & M. Tamura, 717, doi: [10.48550/arXiv.2203.09759](https://doi.org/10.48550/arXiv.2203.09759)
- Dullemond, C. P., Birnstiel, T., Huang, J., et al. 2018, *ApJL*, 869, L46, doi: [10.3847/2041-8213/aaf742](https://doi.org/10.3847/2041-8213/aaf742)
- Epstein, P. S. 1924, *Phys. Rev.*, 23, 710, doi: [10.1103/PhysRev.23.710](https://doi.org/10.1103/PhysRev.23.710)
- Flaherty, K., Hughes, A. M., Simon, J. B., et al. 2020, *ApJ*, 895, 109, doi: [10.3847/1538-4357/ab8cc5](https://doi.org/10.3847/1538-4357/ab8cc5)
- Flaherty, K. M., Hughes, A. M., Teague, R., et al. 2018, *ApJ*, 856, 117, doi: [10.3847/1538-4357/aab615](https://doi.org/10.3847/1538-4357/aab615)
- Flaherty, K. M., Hughes, A. M., Rose, S. C., et al. 2017, *ApJ*, 843, 150, doi: [10.3847/1538-4357/aa79f9](https://doi.org/10.3847/1538-4357/aa79f9)
- Gerbis, K., & Li, R. 2023, *ApJ*, 949, 81, doi: [10.3847/1538-4357/acca1a](https://doi.org/10.3847/1538-4357/acca1a)
- Gerbis, K., Murray-Clay, R. A., Klahr, H., & Baehr, H. 2020, *ApJ*, 895, 91, doi: [10.3847/1538-4357/ab8d37](https://doi.org/10.3847/1538-4357/ab8d37)
- Goldreich, P., & Lynden-Bell, D. 1965, *MNRAS*, 130, 125, doi: [10.1093/mnras/130.2.125](https://doi.org/10.1093/mnras/130.2.125)
- Goldreich, P., & Tremaine, S. 1979, *ApJ*, 233, 857, doi: [10.1086/157448](https://doi.org/10.1086/157448)
- Gundlach, B., & Blum, J. 2015, *ApJ*, 798, 34, doi: [10.1088/0004-637X/798/1/34](https://doi.org/10.1088/0004-637X/798/1/34)
- Güttler, C., Blum, J., Zsom, A., Ormel, C. W., & Dullemond, C. P. 2010, *A&A*, 513, A56, doi: [10.1051/0004-6361/200912852](https://doi.org/10.1051/0004-6361/200912852)
- Haffert, S. Y., Bohn, A. J., de Boer, J., et al. 2019, *Nature Astronomy*, 3, 749, doi: [10.1038/s41550-019-0780-5](https://doi.org/10.1038/s41550-019-0780-5)
- Hammer, M., Kratter, K. M., & Lin, M.-K. 2017, *MNRAS*, 466, 3533, doi: [10.1093/mnras/stw3000](https://doi.org/10.1093/mnras/stw3000)
- Heifetz, E., Bishop, C. H., & Alpert, P. 1999, *Quarterly Journal of the Royal Meteorological Society*, 125, 2835, doi: [10.1002/qj.49712556004](https://doi.org/10.1002/qj.49712556004)
- Hu, X., Li, Z.-Y., Zhu, Z., & Yang, C.-C. 2022, *MNRAS*, 516, 2006, doi: [10.1093/mnras/stac1799](https://doi.org/10.1093/mnras/stac1799)
- Huang, J., Andrews, S. M., Dullemond, C. P., et al. 2018a, *ApJL*, 869, L42, doi: [10.3847/2041-8213/aaf740](https://doi.org/10.3847/2041-8213/aaf740)
- Huang, P., Isella, A., Li, H., Li, S., & Ji, J. 2018b, *ApJ*, 867, 3, doi: [10.3847/1538-4357/aac317](https://doi.org/10.3847/1538-4357/aac317)
- Jennings, J., Booth, R. A., Tazzari, M., Clarke, C. J., & Rosotti, G. P. 2022, *MNRAS*, 509, 2780, doi: [10.1093/mnras/stab3185](https://doi.org/10.1093/mnras/stab3185)
- Jennings, J., Booth, R. A., Tazzari, M., Rosotti, G. P., & Clarke, C. J. 2020, *MNRAS*, 495, 3209, doi: [10.1093/mnras/staa1365](https://doi.org/10.1093/mnras/staa1365)
- Johansen, A., Mac Low, M.-M., Lacerda, P., & Bizzarro, M. 2015, *Science Advances*, 1, 1500109, doi: [10.1126/sciadv.1500109](https://doi.org/10.1126/sciadv.1500109)

- Johansen, A., Oishi, J. S., Mac Low, M.-M., et al. 2007, *Nature*, 448, 1022, doi: [10.1038/nature06086](https://doi.org/10.1038/nature06086)
- Johansen, A., Youdin, A., & Klahr, H. 2009, *ApJ*, 697, 1269, doi: [10.1088/0004-637X/697/2/1269](https://doi.org/10.1088/0004-637X/697/2/1269)
- Keppler, M., Benisty, M., Müller, A., et al. 2018, *A&A*, 617, A44, doi: [10.1051/0004-6361/201832957](https://doi.org/10.1051/0004-6361/201832957)
- Klahr, H., & Schreiber, A. 2020, *ApJ*, 901, 54, doi: [10.3847/1538-4357/abac58](https://doi.org/10.3847/1538-4357/abac58)
- Latter, H. N., & Papaloizou, J. 2017, *MNRAS*, 472, 1432, doi: [10.1093/mnras/stx2038](https://doi.org/10.1093/mnras/stx2038)
- Lesur, G., Flock, M., Ercolano, B., et al. 2023, in *Astronomical Society of the Pacific Conference Series*, Vol. 534, *Astronomical Society of the Pacific Conference Series*, ed. S. Inutsuka, Y. Aikawa, T. Muto, K. Tomida, & M. Tamura, 465
- Li, H., Colgate, S. A., Wendroff, B., & Liska, R. 2001, *ApJ*, 551, 874, doi: [10.1086/320241](https://doi.org/10.1086/320241)
- Li, H., Finn, J. M., Lovelace, R. V. E., & Colgate, S. A. 2000, *ApJ*, 533, 1023, doi: [10.1086/308693](https://doi.org/10.1086/308693)
- Li, R., Youdin, A. N., & Simon, J. B. 2019, *ApJ*, 885, 69, doi: [10.3847/1538-4357/ab480d](https://doi.org/10.3847/1538-4357/ab480d)
- Li, Y.-P., Li, H., Li, S., et al. 2020, *ApJL*, 892, L19, doi: [10.3847/2041-8213/ab7fb2](https://doi.org/10.3847/2041-8213/ab7fb2)
- Lim, J., Simon, J. B., Li, R., et al. 2024, *ApJ*, 969, 130, doi: [10.3847/1538-4357/ad47a2](https://doi.org/10.3847/1538-4357/ad47a2)
- Lin, D. N. C., & Papaloizou, J. 1986, *ApJ*, 309, 846, doi: [10.1086/164653](https://doi.org/10.1086/164653)
- Lin, D. N. C., & Papaloizou, J. C. B. 1993, in *Protostars and Planets III*, ed. E. H. Levy & J. I. Lunine, 749
- Lin, M.-K., & Youdin, A. N. 2017, *ApJ*, 849, 129, doi: [10.3847/1538-4357/aa92cd](https://doi.org/10.3847/1538-4357/aa92cd)
- Liu, H., & Bai, X.-N. 2023, *MNRAS*, 526, 80, doi: [10.1093/mnras/stad2629](https://doi.org/10.1093/mnras/stad2629)
- Lorek, S., Lacerda, P., & Blum, J. 2018, *A&A*, 611, A18, doi: [10.1051/0004-6361/201630175](https://doi.org/10.1051/0004-6361/201630175)
- Lovelace, R. V. E., Li, H., Colgate, S. A., & Nelson, A. F. 1999, *ApJ*, 513, 805, doi: [10.1086/306900](https://doi.org/10.1086/306900)
- Lynch, E. M., & Laibe, G. 2024, *Journal of Fluid Mechanics*, 1001, A37, doi: [10.1017/jfm.2024.1088](https://doi.org/10.1017/jfm.2024.1088)
- Ma, X., Huang, P., Yu, C., & Dong, R. 2024, *arXiv e-prints*, arXiv:2412.11507, doi: [10.48550/arXiv.2412.11507](https://doi.org/10.48550/arXiv.2412.11507)
- Magnan, N., Heinemann, T., & Latter, H. N. 2024, *MNRAS*, 534, 3944, doi: [10.1093/mnras/stae1978](https://doi.org/10.1093/mnras/stae1978)
- Nakagawa, Y., Sekiya, M., & Hayashi, C. 1986, *Icarus*, 67, 375, doi: [10.1016/0019-1035\(86\)90121-1](https://doi.org/10.1016/0019-1035(86)90121-1)
- Ono, T., Muto, T., Takeuchi, T., & Nomura, H. 2016, *ApJ*, 823, 84, doi: [10.3847/0004-637X/823/2/84](https://doi.org/10.3847/0004-637X/823/2/84)
- Paardekooper, S. J., & Mellema, G. 2004, *A&A*, 425, L9, doi: [10.1051/0004-6361:200400053](https://doi.org/10.1051/0004-6361:200400053)
- Pinilla, P., Birnstiel, T., Ricci, L., et al. 2012, *A&A*, 538, A114, doi: [10.1051/0004-6361/201118204](https://doi.org/10.1051/0004-6361/201118204)
- Pinte, C., Teague, R., Flaherty, K., et al. 2023, in *Astronomical Society of the Pacific Conference Series*, Vol. 534, *Protostars and Planets VII*, ed. S. Inutsuka, Y. Aikawa, T. Muto, K. Tomida, & M. Tamura, 645, doi: [10.48550/arXiv.2203.09528](https://doi.org/10.48550/arXiv.2203.09528)
- Riols, A., & Lesur, G. 2019, *A&A*, 625, A108, doi: [10.1051/0004-6361/201834813](https://doi.org/10.1051/0004-6361/201834813)
- Rosotti, G. P. 2023, *NewAR*, 96, 101674, doi: [10.1016/j.newar.2023.101674](https://doi.org/10.1016/j.newar.2023.101674)
- Rosotti, G. P., Teague, R., Dullemond, C., Booth, R. A., & Clarke, C. J. 2020, *MNRAS*, 495, 173, doi: [10.1093/mnras/staa1170](https://doi.org/10.1093/mnras/staa1170)
- Schäfer, U., Johansen, A., Haugbølle, T., & Nordlund, Å. 2024, *A&A*, 691, A258, doi: [10.1051/0004-6361/202450639](https://doi.org/10.1051/0004-6361/202450639)
- Schäfer, U., Yang, C.-C., & Johansen, A. 2017, *A&A*, 597, A69, doi: [10.1051/0004-6361/201629561](https://doi.org/10.1051/0004-6361/201629561)
- Shakura, N. I., & Sunyaev, R. A. 1973, *A&A*, 500, 33
- Simon, J. B., Armitage, P. J., Li, R., & Youdin, A. N. 2016, *ApJ*, 822, 55, doi: [10.3847/0004-637X/822/1/55](https://doi.org/10.3847/0004-637X/822/1/55)
- Simon, J. B., Blum, J., Birnstiel, T., & Nesvorný, D. 2022, *arXiv e-prints*, arXiv:2212.04509, doi: [10.48550/arXiv.2212.04509](https://doi.org/10.48550/arXiv.2212.04509)
- Squire, J., & Hopkins, P. F. 2018a, *MNRAS*, 477, 5011, doi: [10.1093/mnras/sty854](https://doi.org/10.1093/mnras/sty854)
- . 2018b, *ApJL*, 856, L15, doi: [10.3847/2041-8213/aab54d](https://doi.org/10.3847/2041-8213/aab54d)
- Stammler, S. M., Drażkowska, J., Birnstiel, T., et al. 2019, *ApJL*, 884, L5, doi: [10.3847/2041-8213/ab4423](https://doi.org/10.3847/2041-8213/ab4423)
- Toomre, A. 1964, *ApJ*, 139, 1217, doi: [10.1086/147861](https://doi.org/10.1086/147861)
- Umurhan, O. M., Estrada, P. R., & Cuzzi, J. N. 2020, *ApJ*, 895, 4, doi: [10.3847/1538-4357/ab899d](https://doi.org/10.3847/1538-4357/ab899d)
- van der Marel, N., van Dishoeck, E. F., Bruderer, S., et al. 2013, *Science*, 340, 1199, doi: [10.1126/science.1236770](https://doi.org/10.1126/science.1236770)
- van der Marel, N., Birnstiel, T., Garufi, A., et al. 2021, *AJ*, 161, 33, doi: [10.3847/1538-3881/abc3ba](https://doi.org/10.3847/1538-3881/abc3ba)
- Weidenschilling, S. J. 1977, *Ap&SS*, 51, 153, doi: [10.1007/BF00642464](https://doi.org/10.1007/BF00642464)
- Xu, Z., & Bai, X.-N. 2022a, *ApJ*, 924, 3, doi: [10.3847/1538-4357/ac31a7](https://doi.org/10.3847/1538-4357/ac31a7)
- . 2022b, *ApJL*, 937, L4, doi: [10.3847/2041-8213/ac8dff](https://doi.org/10.3847/2041-8213/ac8dff)
- Yang, C.-C., Johansen, A., & Carrera, D. 2017, *A&A*, 606, A80, doi: [10.1051/0004-6361/201630106](https://doi.org/10.1051/0004-6361/201630106)
- Yang, L., Li, Y.-P., Dong, R., et al. 2025, *arXiv e-prints*, arXiv:2503.13818, doi: [10.48550/arXiv.2503.13818](https://doi.org/10.48550/arXiv.2503.13818)
- Youdin, A. N., & Goodman, J. 2005, *ApJ*, 620, 459, doi: [10.1086/426895](https://doi.org/10.1086/426895)
- Youdin, A. N., & Lithwick, Y. 2007, *Icarus*, 192, 588, doi: [10.1016/j.icarus.2007.07.012](https://doi.org/10.1016/j.icarus.2007.07.012)

Zhu, Z., & Stone, J. M. 2014, ApJ, 795, 53,
doi: [10.1088/0004-637X/795/1/53](https://doi.org/10.1088/0004-637X/795/1/53)

Zhu, Z., Stone, J. M., Rafikov, R. R., & Bai, X.-n. 2014,
ApJ, 785, 122, doi: [10.1088/0004-637X/785/2/122](https://doi.org/10.1088/0004-637X/785/2/122)

Zsom, A., Ormel, C. W., Güttler, C., Blum, J., &
Dullemond, C. P. 2010, A&A, 513, A57,
doi: [10.1051/0004-6361/200912976](https://doi.org/10.1051/0004-6361/200912976)

APPENDIX

A. STEADY STATE DUST DENSITY

In §2.4.1, we derive the steady state solutions in the non-drift regime. Given $v_{\text{gy}0} = v_{\text{dy}0}$, it requests that the dust diffusion term in equation (15) and the gas pressure gradient in equation (13) to be equal. This yields the following second order ordinary differential equation,

$$\frac{1}{\rho_{\text{d}0}} \frac{\partial}{\partial x} [\rho_{\text{d}0} D_{\text{d}}^2 (\partial \ln \epsilon_0 / \partial x)^2] + \frac{1}{\rho_{\text{g}0}} \frac{\partial P_0}{\partial x} = 0. \quad (\text{A1})$$

We solve A1 numerically as an initial value problem. We first convert it to two first order ODEs, by defining

$$y_1 = \epsilon_0, \quad (\text{A2})$$

$$y_2 = \frac{\partial \ln \epsilon_0}{\partial x}. \quad (\text{A3})$$

Then, A1 is cast into

$$dy_1 = y_1 y_2, \quad (\text{A4})$$

$$dy_2 = -\frac{1}{2} \left[y_2^2 + y_2 \frac{\partial \ln \rho_{\text{g}0}}{\partial x} + \frac{1}{y_2} \frac{1}{D_{\text{d}}^2 \rho_{\text{g}0}} \frac{\partial P_0}{\partial x} \right]. \quad (\text{A5})$$

We expect a Gaussian bump for dust density. This agrees with the continuum observations of rings and gaps in ALMA (Huang et al. 2018a; Andrews 2020). Hence, the initial conditions are given by

$$y_1(x=0) = \epsilon_{\text{max}}, \quad (\text{A6})$$

$$y_2(x=0) = 0. \quad (\text{A7})$$

In practice, we note that y_2 appears in the denominator of A5. To avoid the singularity at $x=0$, we opt for integrating the ODEs in the domain of $x \in [x_{\text{min}}, 4H]$, where $x_{\text{min}} = 10^{-10}H$. To find y_2 at $x = x_{\text{min}}$, we take the limit of $x \rightarrow 0$ of A5. With L'Hospital's rule, we arrive at

$$\left. \frac{dy_2}{dx} \right|_{x=0} = -\frac{1}{2D_{\text{d}}(1+A)} \frac{\left. \frac{d^2 P_0}{dx^2} \right|_{x=0}}{\left. \frac{dy_2}{dx} \right|_{x=0}}. \quad (\text{A8})$$

This is a quadratic equation in $\left. \frac{dy_2}{dx} \right|_{x=0}$, and we take the negative root as at $x=0$, $\epsilon = \epsilon_{\text{max}}$. Thus, the boundary conditions at $x = x_{\text{min}}$ are

$$y_1(x = x_{\text{min}}) = \epsilon_{\text{max}}, \quad (\text{A9})$$

$$y_2(x = x_{\text{min}}) = x_{\text{min}} \left. \frac{dy_2}{dx} \right|_{x=0}. \quad (\text{A10})$$

A4 and A5 are solved by `scipy.integrate.odeint`, which uses LSODA from the FORTRAN library odepack.

B. BOUNDARY CONDITIONS AND FOURIER BASIS

Density waves can appear in the eigenfunctions of (D)RWI. They are launched at the Lindblad resonances and propagate away from the pressure bump (Li et al. 2000). Previous work on the linear analysis of RWI typically employed boundary conditions to accommodate density waves (Ono et al. 2016, LB23). This is achieved by applying WKB analysis in x at the boundaries, where the steady-state quantities vary slowly, and the eigenfunctions are expressed as $\propto \exp(ik_x x + ik_y y - i\omega t)$. However, this approach involves the computation of k_x at the boundaries, adding complexity to solving the EVPs (see Appendix A2 of LB23). In this work, we adopt the Fourier basis, which naturally satisfies periodic boundary conditions. This choice is motivated by its simplicity, as there is no need to compute k_x at the boundaries. Below, using the numerical method described in §2, we demonstrate that 1) the Fourier

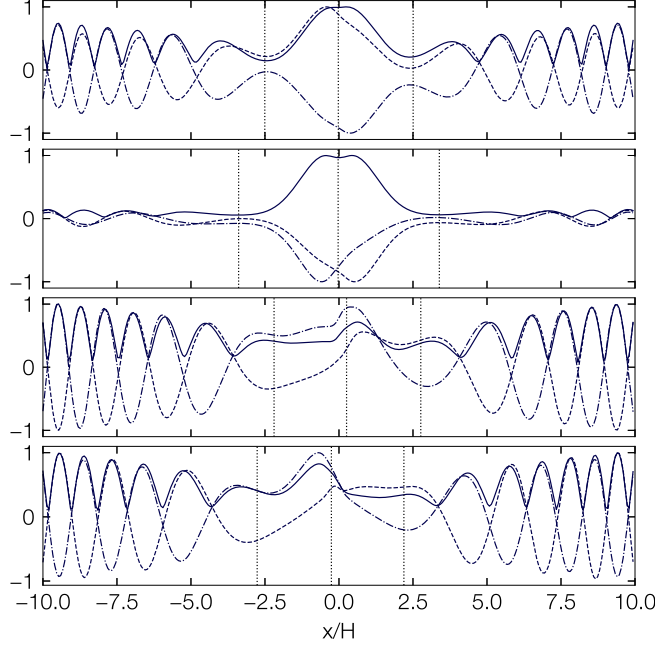


Figure 15. Normalized real (dashed), imaginary (dash-dotted), and absolute (solid) part of the perturbed gas density in the domain of $x/H \in [-10, 10]$. The vertical blue lines show the corotation, inner and outer Lindblad radii. First row: gas RWI with parameters $H/r_0 = 0.1$, $A = 1.5$, $w = H$, $\alpha = 10^{-3}$, $k_y r_0 = 3$, $x_c/H = -0.022$, $x_{\text{ILR}}/H = -2.505$, $x_{\text{OLR}}/H = 2.505$. Second row: Type I RWI mode with parameters $k_y r_0 = 2$, $\epsilon = 0.5$, $w_d = 0.05$, $\text{St} = 0.01$, $x_c/H = -0.0285$, $x_{\text{ILR}}/H = -3.39$, $x_{\text{OLR}}/H = 3.39$. Third and fourth rows: a pair of Type II RWI modes with parameters $k_y r_0 = 3$, $\epsilon = 0.5$, $w_d = 0.3$, $\text{St} = 0.01$, $x_c/H = 0.256, -0.256$, $x_{\text{ILR}}/H = -2.193, 2.193$, $x_{\text{OLR}}/H = 2.764, -2.764$.

basis effectively captures density waves, and 2) whether or not density waves are included in the domain has little impact on the growth rates of (D)RWI.

Figure 15 shows the normalized perturbed gas density $\delta\rho_g$, for the pure gas RWI, Type I, and a pair of Type II modes, respectively (from top to bottom). The corotation radius x_c , where $\text{Re}[\Delta\omega] = 0$ and the inner and outer Lindblad radii x_{ILR} , x_{OLR} , where $\Delta\omega^2 = \kappa^2$ and $\kappa^2 = 2\Omega(2\Omega + \partial v_{\text{gy}0}/\partial x)$, are shown as vertical lines. The radial domain is extended to $x/H \in [-10, 10]$ in Figure 15 in order to accommodate the density waves. It is clear that in all the panels density waves are captured. The growth rates from top to bottom panel are $\gamma/\Omega = 0.039, 0.084, 0.037, 0.037$, respectively. Now, we test with the domain of $x/H \in [-4, 4]$ employed in the main text. Density waves do not propagate far, yet the growth rates remain largely unaffected, with $\gamma/\Omega = 0.041, 0.083, 0.039, 0.039$, respectively. The reason behind is (D)RWI structure is concentrated around $x = 0$, whereas density waves emerge farther from the domain center, and hence have little impact on the (D)RWI.

C. VORTENSITY EQUATION

To understand the DRWI mechanism, we shall investigate how the background vortensity is transferred to Rossby waves. This is done by deriving the vortensity equation. Taking the curl of eq. (3), we have

$$\frac{\partial \zeta}{\partial x} + \nabla \times (\zeta \times \mathbf{v}_g) = \nabla \times [-2\mathbf{\Omega} \times \mathbf{v}_g + 3\Omega^2 x \mathbf{e}_x] + \mathbf{S}, \quad (\text{C11})$$

and the source terms are

$$\mathbf{S} = \nabla \times \left[-\frac{\nabla P}{\rho_g} + \frac{\epsilon}{t_s}(\mathbf{v}_d - \mathbf{v}_g) + \nu \nabla^2 \mathbf{v}_g + F(x) \mathbf{e}_y \right]. \quad (\text{C12})$$

They correspond to baroclinity, drag force, gas viscosity, and forcing, respectively. By noting that

$$\nabla \times (\zeta \times \mathbf{v}_g) = (\mathbf{v}_g \cdot \nabla) \zeta + \zeta (\nabla \cdot \mathbf{v}_g), \quad (\text{C13})$$

and

$$\nabla \times [-2\mathbf{\Omega} \times \mathbf{v}_g + 3\Omega^2 x \mathbf{e}_x] = -2\mathbf{\Omega} (\nabla \cdot \mathbf{v}_g), \quad (\text{C14})$$

and that all terms in C11 are in z -direction, we arrive at

$$\frac{Dq}{Dt} = \frac{S}{\rho_g}, \quad (\text{C15})$$

where $D/Dt = \partial/\partial t + \mathbf{v}_g \cdot \nabla$ is the material derivative. Then, the perturbed vortensity equation is

$$(-i\omega + ik_y v_{gy0})\delta q + \delta v_{gx} \frac{\partial q_0}{\partial x} = S', \quad (\text{C16})$$

where

$$S' = S'_{\text{drag}} + S'_{\text{visc}} + S'_{\text{forc}}. \quad (\text{C17})$$

Different from LB23, the equation of state in this work is barotropic, and hence no baroclinic term involved in the perturbed vortensity equation. In practice, the viscosity and forcing terms are much smaller than the drag force term, and

$$S' \approx S'_{\text{drag}} = \frac{1}{\rho_g} \frac{\epsilon}{t_s} \nabla \times (\delta \mathbf{v}_d - \delta \mathbf{v}_g). \quad (\text{C18})$$

Following a similar derivation and utilizing equation (4), we obtain the dust vortensity equation,

$$\frac{Dq_d}{Dt} = \frac{S_d}{\rho_d}, \quad (\text{C19})$$

where

$$\mathbf{S}_d = \nabla \times \left[-\frac{1}{t_s} (\mathbf{v}_d - \mathbf{v}_g) + \frac{1}{\rho_d} \nabla \cdot (\rho_d \mathbf{v}_{\text{dif}} \mathbf{v}_{\text{dif}}) \right]. \quad (\text{C20})$$

The perturbed dust vortensity equation is

$$(-i\omega + ik_y v_{dy0})\delta q_d + \delta v_{dx} \frac{\partial q_{d0}}{\partial x} = S'_d. \quad (\text{C21})$$

The drag force term dominates over the dust diffusion term for S'_d ,

$$S'_d \approx S'_{d,\text{drag}} = -\frac{1}{\rho_d t_s} \nabla \times (\delta \mathbf{v}_d - \delta \mathbf{v}_g). \quad (\text{C22})$$